Journal of Computational Physics 227 (2008) 9365–9388

Contents lists available at ScienceDirect

Journal of Computational Physics

journal homepage: www.elsevier.com/locate/jcp

A finite volume method for the approximation of Maxwell's equations in two space dimensions on arbitrary meshes

F. Hermeline [a], S. Layouni [b], P. Omnes [b,*]

[a] Commissariat à l'énergie atomique, Centre DAM-Ile de France, DSSI, Bruyères-le-Châtel, 91297 Arpajon Cedex, France
[b] CEA Saclay, DEN/DM2S/SFME, 91191 Gif Sur Yvette Cedex, France

ARTICLE INFO

Article history:
Received 27 August 2007
Received in revised form 16 May 2008
Accepted 23 May 2008
Available online 26 August 2008

Keywords:
Finite volume method
Maxwell's equations
Dual mesh
Non-conforming meshes
Distorted meshes
Gauss' law
Divergence free fields
Energy conservation
CFL stability condition

ABSTRACT

A new finite volume method is presented for discretizing the two-dimensional Maxwell equations. This method may be seen as an extension of the covolume type methods to arbitrary, possibly non-conforming or even non-convex, *n*-sided polygonal meshes, thanks to an appropriate choice of degrees of freedom. An equivalent formulation of the scheme is given in terms of discrete differential operators obeying discrete duality principles. The main properties of the scheme are its energy conservation, its stability under a CFL-like condition, and the fact that it preserves Gauss' law and divergence free magnetic fields. Second-order convergence is demonstrated numerically on non-conforming and distorted meshes.

© 2008 Elsevier Inc. All rights reserved.

1. Introduction

The finite-difference time-domain (FDTD) method is a widely used numerical technique to approach the solution of the time-dependent Maxwell equations. In its original formulation, as proposed by Yee [1], this scheme is written on a uniform Cartesian grid, which is of course a severe restriction for its use in modern engineering issues. Therefore, this scheme has known numerous developments and generalizations that extend its use to complex geometries and unstructured or locally refined meshes. For a recent review of these developments, we refer the reader to [2].

One of these generalizations is the so-called "control region" or "covolume" scheme, proposed in [3–6] and analyzed for the time-domain equations in [7,8]. The covolume scheme employs Voronoi–Delaunay mesh pairs to replace the rectangular staggered meshes of Yee's scheme. Restricting to two-dimensional meshes for the sake of clarity and to the transverse magnetic (TM) mode (although the discussion also holds for the transverse electric mode), the unknowns of this scheme are the values of the magnetic field at the centers of the cells of the primal mesh, and the tangential components of the electric field along the sides of the primal mesh. Then, Faraday's law is integrated over the primal cells and the tangential component of Ampère's law is integrated along the sides of the dual mesh.

* Corresponding author. Tel.: +33 1 69 08 43 57; fax: +33 1 69 08 10 87.
E-mail addresses: francois.hermeline@cea.fr (F. Hermeline), siham.layouni@cea.fr (S. Layouni), pascal.omnes@cea.fr (P. Omnes).

0021-9991/$ - see front matter © 2008 Elsevier Inc. All rights reserved.
doi:10.1016/j.jcp.2008.05.013

A first advantage of this scheme is that it may be applied to more general domains of $\mathbb{R}^2$ or $\mathbb{R}^3$ and to a much wider class of meshes than Yee's scheme. However, the orthogonality relation between the two meshes sets a limitation to the use of the method, particularly in the context of mesh refinement or coarsening, since these processes may lead to non-conforming cells. A second advantage of this scheme is that the magnetic field remains divergence free and that a discrete equivalent of Gauss' law holds, provided the charge and current densities that act as source terms in the Maxwell equations verify a discrete analogue of the charge conservation equation. This point was addressed in [6]. A third advantage is that the method is non-dissipative since it can be proved that a discrete analogue of the electromagnetic energy is conserved as soon as the media is itself non-dissipative. Finally, the method has been proved to be first-order convergent in [7] for general grids and second-order convergent for Cartesian rectangular grids.

In this article, we propose a generalization of the covolume scheme to two-dimensional non-orthogonal (almost) arbitrary meshes, including in particular meshes with non-conforming or non-convex cells. For the TM mode, the unknowns of our scheme are the values of the magnetic field at the centers of the cells of *both* the primal and dual cells, as well as *both* components of the electric field on the sides of the primal and dual meshes. The discretization is simply performed by integrating Faraday's law on the cells of *both* the primal and dual meshes and by integrating *both* components of Ampère's law over the sides of the mesh. The above-mentioned advantages of the covolume scheme are preserved through this extension. Moreover, the scheme can be proved to be conditionally stable under a CFL-like condition which degenerates to the usual stability condition of Yee's scheme on regular Cartesian grids. The scheme easily extends to anisotropic media with discontinuous permittivity and permeability tensors. Our numerical tests also show that the results are highly independent of the mesh skewness or non-conformity.

Of course, there are other schemes which share advantages of that presented here. We may cite for example finite element time domain methods which may be applied on unstructured meshes and may preserve a discrete energy when properly time-discretized. The reader is referred for example to [9] for edge elements and to [10,11] for nodal elements. However, their use on non-conforming locally refined meshes requires the introduction of Lagrange multipliers (see for example [12,13] for space refinement only and [14–16] for space–time refinement); moreover, the efficient implementation of edge elements require lumping of mass matrices, which is still the subject of significant research (see for example [17]). The ability of finite element methods to preserve globally divergence free field (or Gauss' law) is also questionable if care is not taken in the variational formulation [18–20] and a correction step [10] may be required. Finite volume ideas borrowed from the field of computational fluid dynamics (hereafter named FVCFD) have also been used over the past fifteen years to gain flexibility in the meshes used and robustness in the presence of strong gradients [21–25]. However, the preservation of Gauss' law also requires special treatments [26–28] which make the computations heavier, and these methods fail in conserving a discrete energy; this numerical dissipation limits their use to relatively short-time computations. More recently, finite volume methods that preserve a discrete energy have been developed in [29,30] and can be used on very general grids. However, on Cartesian square grids of spatial dimension $d = 1$, 2 or 3, with mesh step size h, this scheme reduces to 2^d Yee schemes on 2^d staggered grids of mesh step size $2h$. Thus, in order to obtain an equivalent accuracy as that of Yee's scheme, one has to use grids which are twice finer in each direction, which implies of course much greater computer costs. To improve accuracy on a given grid, this finite volume method has been generalized in [31] to yield a discontinuous Galerkin time domain (DGTD) method of arbitrary order of accuracy (see also [32] for its use on Cartesian locally refined grids). Note however that, as usual with higher-order methods, the improvement in the order of convergence is limited by the regularity of the solution itself; this is a fundamental issue since in the presence of non-convex domains with reentrant corners (a situation which is often met in practical engineering problems) the solution of Maxwell's equations is singular (see [33]). Various ways have been proposed to overcome this loss of accuracy due to singularities. In the context of time-harmonic solutions, we may cite h/p adaptivity [34–37] and weighted regularization techniques [38]. As far as the time-dependent problem is concerned, weighted regularization techniques [39] and the singular complement method [40,41] have been used, but, to our knowledge, have not been extended so far to convergence orders greater than one. This clearly shows that there is still a need for efficient low order methods. In addition, in the DGTD methods considered in [31,32], conservation of the divergence free character of the fields is ensured only in a weak sense, and nothing is said about the possible violation of Gauss' law in the presence of charge and current densities. Another approach proposed in [42] is to use a DGTD method with locally divergence free basis functions together with a projection on globally divergence free functions, but of course this method should be reconsidered in the case of non-vanishing charge and current densities. Moreover, this method is based on upwind fluxes like FVCFD methods, and does not exactly preserve a discrete energy, although a modification of this method in order to use centered fluxes in the spirit of [31,32] may be considered. Another DGTD method based on standard node-based piecewise polynomial spaces (which limits its use to simplices only) may be found in [43], where the divergence free character of the fields is left to the accuracy of the solver. In the presence of charge and current densities, the scheme has to be corrected, involving heavier computations [44]. Finally, we may also cite [45,46] in which discontinuous Galerkin methods over space–time simplices are presented and analyzed. These methods have the advantage of having local stability constraints (larger elements use larger time-steps), but nothing is said concerning the preservation of Gauss' law or the conservation of a discrete energy.

The scheme we present is an extension to Maxwell's equations of two visions of recent ideas that were developed by the authors to approach diffusion equations and related problems. In [47–50], a finite volume method was presented for the approximation of diffusion equations on distorted meshes; it is based on a geometric approach of finite volumes. On the other hand, in [51–53], equivalent schemes were designed based on the derivation of discrete differential operators like

divergence, gradient and curl. Since these discrete operators satisfy discrete analogues of the Green formula, this class of methods has been named "discrete duality finite volume (DDFV)" methods. These discrete operators also share properties verified by the continuous operators, like the existence of a discrete Hodge decomposition of vector fields and the property that the divergence of a curl vanishes. This is a key ingredient in proving that the present scheme verifies Gauss' law. These properties show that our scheme is strongly related to the so-called "generalized finite differences" approach, see [54] and the numerous references therein. However, in the DDFV method, the "discrete Hodge operator" ε (we use here the terminology of [54]), which relates the discrete electric field $\boldsymbol{E}$ to the discrete electric displacement $\boldsymbol{D}$ by the relation $\boldsymbol{D} = \varepsilon \boldsymbol{E}$, is diagonal *even if the primal and dual meshes are not orthogonal*. This is a great advantage over methods related to that presented in [54], since we avoid the whole Whitney form machinery and the induced interpolations. We mention that DDFV methods have been successfully applied to non-linear diffusion problems [48,55], drift-diffusion and energy-transport models [56,57] and to the 2-D and 3-D bi-domain equations of electro-cardiology [58]. In the present work, we show that both visions, as developed in [47–50,59] on the one hand and in [51–53] on the other hand can be used to construct the scheme and to prove its properties.

The extension of our method to three-space dimensions is not straightforward. Several ways can be investigated and we have not tested so far which of these could provide the best numerical results. One such way is outlined in the Appendix.

The organization of the paper is as follows. Section 2 is devoted to the definition of what we call the primal and dual meshes and the related notations. Section 3 is concerned with the Maxwell equations in two space dimensions. The proposed method is set out in Section 4 in the general framework of inhomogeneous media. Section 5 describes a slightly different point of view based on the discretization of the involved differential operators. For the sake of simplicity this point of view has been detailed for a homogeneous medium. Then, in Section 6, we compare the stability constraint and the complexity of the present method with those of other techniques. Finally, several numerical experiments are presented in Section 7.

2. Primal and dual meshes: definitions and notations

Given Ω, a bounded polygonal domain, we consider a mesh on Ω (called primal mesh) made up of arbitrary (possibly distorted, non-conforming or non-convex) n-sided polygons. With each (primal) element P_p of this mesh we associate one (primal) point ξ_p: the centroid is a qualified candidate but other points could be chosen. By connecting these primal points and the midpoints ξ_s of the sides, we obtain a second mesh on Ω (called indirect dual mesh: see Fig. 1).

With each (dual) element Π_d of this mesh, we can associate one vertex of the primal mesh that will be denoted by $\boldsymbol{x}_d$.

In addition to the indirect dual mesh, other possible definitions of the dual mesh could be used such as the two following ones:

1. The most simple example is the so-called direct dual mesh, obtained by connecting only the primal points. Fig. 2 (bottom-left) displays a 2-D sample of such a dual mesh.

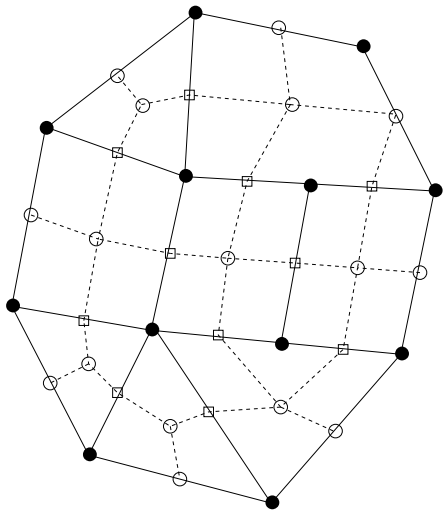

Fig. 1. A sample 2-D non-conforming primal mesh (solid lines) and its associated indirect dual mesh (dashed lines).

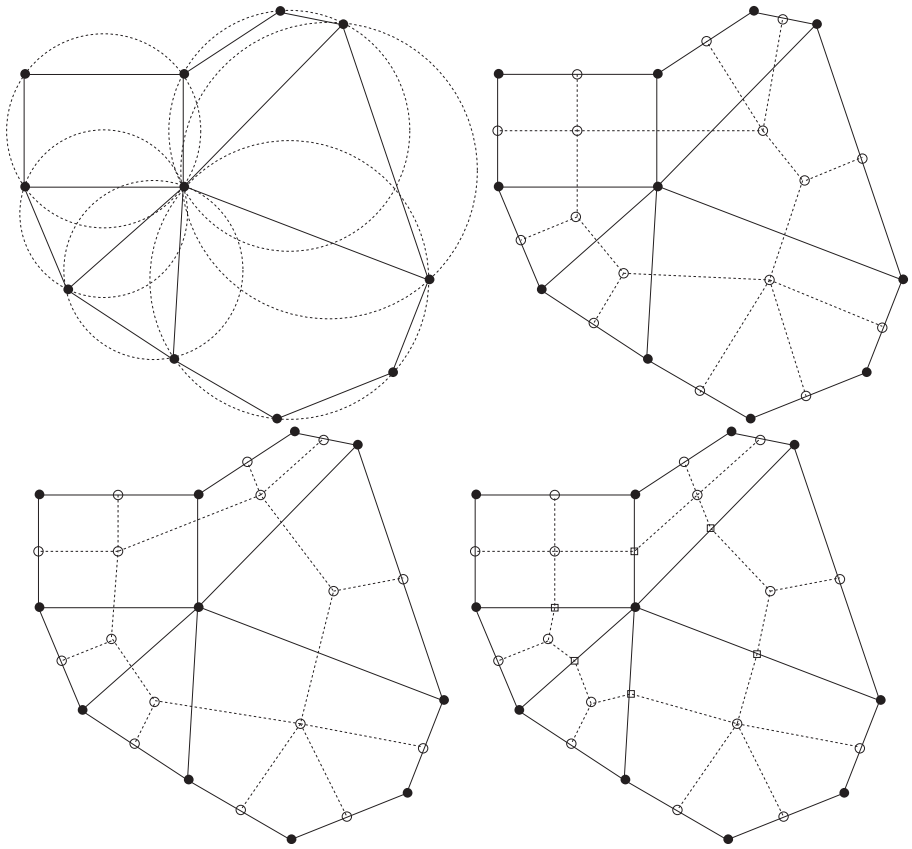

Fig. 2. A sample Delaunay primal mesh made up of three triangles, two quadrilaterals and one pentagon, all inscribed in a ball, (solid lines, top-left) and its Voronoi dual mesh (dashed lines, top-right), its direct dual mesh (dashed lines, bottom-left) and its indirect dual mesh (dashed lines, bottom right). Unlike the Voronoi dual mesh note that the direct and the indirect dual meshes may always be defined, even if the primal mesh is not a Delaunay mesh.

2. The second important example is the Voronoi mesh. Assume that each primal polygon can be inscribed in an open ball that does not contain any vertex (that is to say the primal mesh is a Delaunay mesh: see Fig. 2(top-left)). If all the ball centers are contained in Ω, they can be chosen to be the primal interior points, although some of them may not belong to their primal cell. By connecting these primal points and the primal boundary points, we obtain the so-called Voronoi dual mesh, whose sides are perpendicular to the primal sides. Fig. 2(top-right) displays a 2-D sample of Voronoi mesh. For more precisions see [60–63] and the bibliographies mentioned therein.

In the following we (incorrectly) define a "side" as being the one-dimensional boundary shared by two polygons. In consequence of this definition one notice that the vertices of a dual side need not be collinear (see for example the side Σ_s in Fig. 3).

For the sake of clarity the geometrical objects related to the primal (dual) mesh are denoted by roman (Greek) letters and the vectors are denoted in bold.

Let us denote by (Fig. 3):

- $P_p(\Pi_d)$ the primal (dual) polygon associated with the point $\xi_p(\boldsymbol{x}_d)$,
- $\|P_p\|(\|\Pi_d\|)$ the area of $P_p(\Pi_d)$,
- $S_s = \boldsymbol{x}_d\boldsymbol{x}_e(\Sigma_{sp} = \xi_p\xi_s, \Sigma_{sq} = \xi_s\xi_q, \Sigma_s = \xi_p\xi_s\xi_q)$ the side(s) of a primal (dual) polygon,
- $|S_s|(|\Sigma_{sp}|, |\Sigma_{sq}|, |\Sigma_s| = |\Sigma_{sp}| + |\Sigma_{sq}|)$ the length of $S_s(\Sigma_{sp}, \Sigma_{sq}, \Sigma_s)$,
- Q_s the quadrilateral $\xi_p\boldsymbol{x}_d\xi_q\boldsymbol{x}_e$ (often called diamond cell) associated with S_s and Σ_s,
- $Q_{sp}(Q_{sq})$ the degenerate quadrilateral $\xi_p\boldsymbol{x}_d\xi_s\boldsymbol{x}_e(\xi_q\boldsymbol{x}_e\xi_s\boldsymbol{x}_d)$,
- $\|Q_s\|, \|Q_{sp}\|, \|Q_{sq}\|$ the areas of Q_s, Q_{sp}, Q_{sq},
- $\boldsymbol{n}_s$ the unit outward normal vector on the side S_s of P_p,
- $\boldsymbol{t}_s$ the unit counterclockwise tangent vector on the side S_s of P_p,

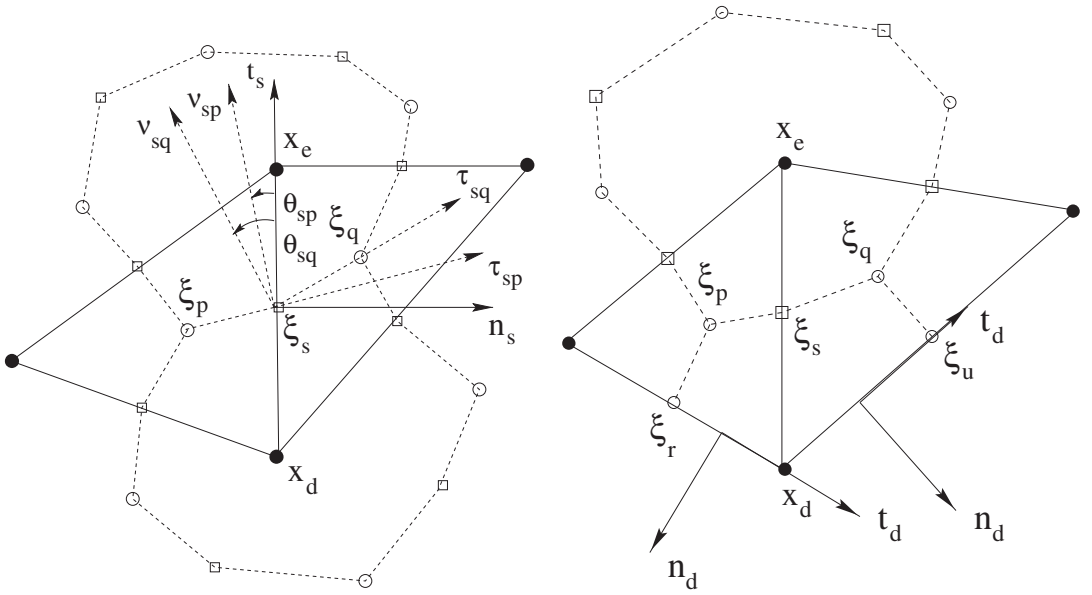

Fig. 3. Two primal (dual) polygons $P_p, P_q(\Pi_d, \Pi_e)$ sharing the side $S_s = \boldsymbol{x}_d\boldsymbol{x}_e(\Sigma_s = \Sigma_{sp} \cup \Sigma_{sq} = \xi_p\xi_s\xi_q)$. The dual polygon Π_d may be either an interior one (left) or a boundary one (right).

- $\boldsymbol{\nu}_{sp}(\boldsymbol{\nu}_{sq})$ the unit outward normal vector on the side $\Sigma_{sp}(\Sigma_{sq})$ of Π_d,
- $\boldsymbol{\tau}_{sp}(\boldsymbol{\tau}_{sq})$ the unit clockwise tangent vector on the side $\Sigma_{sp}(\Sigma_{sq})$ of Π_d,
- $\theta_{sp}(\theta_{sq})$ the angle between $\boldsymbol{t}_s$ and $\boldsymbol{\nu}_{sp}(\boldsymbol{\nu}_{sq})$,
- $c_{sp} = \cos\theta_{sp}(c_{sq} = \cos\theta_{sq})$ and $s_{sp} = \sin\theta_{sp}(s_{sq} = \sin\theta_{sq})$,
- $c_s = \frac{c_{sp}|\Sigma_{sp}| + c_{sq}|\Sigma_{sq}|}{|\Sigma_{sp}| + |\Sigma_{sq}|}$ and $s_s = \frac{s_{sp}|\Sigma_{sp}| + s_{sq}|\Sigma_{sq}|}{|\Sigma_{sp}| + |\Sigma_{sq}|}$.

One can note that

$$\|Q_{sp}\| = \frac{1}{2}c_{sp}|S_s|\|\Sigma_{sp}|, \quad \|Q_{sq}\| = \frac{1}{2}c_{sq}|S_s|\|\Sigma_{sq}|, \tag{1}$$

$$\|Q_s\| = \|Q_{sp}\| + \|Q_{sq}\| = \frac{1}{2}c_s|S_s|\|\Sigma_s|, \tag{2}$$

$$\boldsymbol{\nu}_{sp} = c_{sp}\boldsymbol{t}_s - s_{sp}\boldsymbol{n}_s, \quad \boldsymbol{\nu}_{sq} = c_{sq}\boldsymbol{t}_s - s_{sq}\boldsymbol{n}_s, \tag{3}$$

$$\boldsymbol{\tau}_{sp} = c_{sp}\boldsymbol{n}_s + s_{sp}\boldsymbol{t}_s, \quad \boldsymbol{\tau}_{sq} = c_{sq}\boldsymbol{n}_s + s_{sq}\boldsymbol{t}_s. \tag{4}$$

3. Maxwell's equations

Let us denote by

- $\boldsymbol{x} = (x, y)$ the position and t the time,
- $\rho = \rho(\boldsymbol{x}, t)$ the charge density,
- $\boldsymbol{j} = \boldsymbol{j}(\boldsymbol{x}, t) = (j_x(\boldsymbol{x}, t), j_y(\boldsymbol{x}, t))$ and $j = j_z(\boldsymbol{x}, t)$ the current density and the perpendicular current density,
- $\varepsilon = \varepsilon(\boldsymbol{x})$ and $\mu = \mu(\boldsymbol{x})$ the electric permittivity and the magnetic permeability,
- $\boldsymbol{H} = \boldsymbol{H}(\boldsymbol{x}, t) = (H_x(\boldsymbol{x}, t), H_y(\boldsymbol{x}, t))$ and $\boldsymbol{B} = \mu\boldsymbol{H} = (B_x(\boldsymbol{x}, t), B_y(\boldsymbol{x}, t))$ the magnetic field and the magnetic induction,
- $H = H_z(\boldsymbol{x}, t)$ and $B = \mu H = B_z(\boldsymbol{x}, t)$ the perpendicular magnetic field and the perpendicular magnetic induction,
- $\boldsymbol{E} = (E_x(\boldsymbol{x}, t), E_y(\boldsymbol{x}, t))$ and $\boldsymbol{D} = \varepsilon\boldsymbol{E} = (D_x(\boldsymbol{x}, t), D_y(\boldsymbol{x}, t))$ the electric field and the displacement current,
- $E = E_z(\boldsymbol{x}, t)$ and $D = \varepsilon E = D_z(\boldsymbol{x}, t)$ the perpendicular electric field and the perpendicular displacement current,
- $\boldsymbol{t}$ the unit counterclockwise tangent vector along the boundary $\partial\Omega$,
- $\alpha = \alpha(\boldsymbol{x}), \beta = \beta(\boldsymbol{x})$ positive functions defined on $\partial\Omega$,
- $g = g(\boldsymbol{x})$ a function defined on $\partial\Omega$.

Given u and $\boldsymbol{v} = (v_x, v_y)$ a scalar and a vector function, we denote

$$\nabla u = \left(\frac{\partial u}{\partial x}, \frac{\partial u}{\partial y}\right), \quad \nabla \times u = \left(\frac{\partial u}{\partial y}, -\frac{\partial u}{\partial x}\right)$$

and

$$\nabla \cdot \boldsymbol{v} = \frac{\partial v_x}{\partial x} + \frac{\partial v_y}{\partial y}, \quad \nabla \times \boldsymbol{v} = \frac{\partial v_y}{\partial x} - \frac{\partial v_x}{\partial y}.$$

The fields $H, B, \boldsymbol{E}, \boldsymbol{D}$ are solutions to the 2-D Maxwell equations in the transverse magnetic mode of polarization

$$\begin{cases} \frac{\partial B}{\partial t} + \nabla \times \boldsymbol{E} = 0 & \text{in } [0,T] \times \Omega \quad \text{(Faraday's law)}, \\ \frac{\partial \boldsymbol{D}}{\partial t} - \nabla \times H = -\boldsymbol{j} & \text{in } [0,T] \times \Omega \quad \text{(Ampere—Maxwell's law)}, \\ \nabla \cdot \boldsymbol{D} = \rho & \text{in } [0,T] \times \Omega \quad \text{(Gauss' law)}, \\ \alpha \boldsymbol{E} \cdot \boldsymbol{t} - \beta H = g & \text{on } [0,T] \times \partial\Omega, \end{cases} \tag{5}$$

while the fields $\boldsymbol{H}, \boldsymbol{B}, E, D$ are solutions to the 2-D Maxwell equations in the transverse electric mode of polarization

$$\begin{cases} \frac{\partial \boldsymbol{B}}{\partial t} + \nabla \times E = 0 & \text{in } [0,T] \times \Omega \quad \text{(Faraday's law)}, \\ \frac{\partial D}{\partial t} - \nabla \times \boldsymbol{H} = -j & \text{in } [0,T] \times \Omega \quad \text{(Ampere—Maxwell's law)}, \\ \nabla \cdot \boldsymbol{B} = 0 & \text{in } [0,T] \times \Omega, \\ \alpha E + \beta \boldsymbol{H} \cdot \boldsymbol{t} = g & \text{on } [0,T] \times \partial\Omega. \end{cases} \tag{6}$$

Note that the following boundary conditions:

- perfect conductor ($\alpha = 1, \beta = 0, g = 0$),
- magnetic wall ($\alpha = 0, \beta = 1, g = 0$),
- Silver–Muller condition ($\alpha = 1$, $\beta = \varepsilon^{-\frac{1}{2}}\mu^{\frac{1}{2}}$)

are embodied in the quite general last equation of (5) and (6). Let us recall that the third equation of (5) (Gauss' law) is satisfied at any time, provided it is satisfied at the initial time and if the charge conservation law

$$\frac{\partial \rho}{\partial t} + \nabla \cdot \boldsymbol{j} = 0 \quad \text{in } [0,T] \times \Omega$$

holds. Similarly the third equation of (6) is satisfied at any time, provided it is satisfied at the initial time.

If U and $\boldsymbol{S}$ stand for the electromagnetic energy density and the Poynting vector

$$U = \frac{1}{2}(\boldsymbol{D} \cdot \boldsymbol{E} + BH) \quad \text{and} \quad \boldsymbol{S} = \boldsymbol{E} \times H = H_z(E_y, -E_x),$$

the energy equation associated with (5) reads

$$\frac{\partial U}{\partial t} + \nabla \cdot \boldsymbol{S} = -\boldsymbol{j} \cdot \boldsymbol{E}, \tag{7}$$

while the energy equation associated with (6) would read

$$\frac{\partial \widetilde{U}}{\partial t} + \nabla \cdot \widetilde{\boldsymbol{S}} = -jE$$

with

$$\widetilde{U} = \frac{1}{2}(DE + \boldsymbol{B} \cdot \boldsymbol{H}) \quad \text{and} \quad \widetilde{\boldsymbol{S}} = E \times \boldsymbol{H} = E_z(-H_y, H_x).$$

4. Approximation of the Maxwell equations

Let us focus on Eq. (5). In what follows, we will suppose that $H, \boldsymbol{E} \cdot \boldsymbol{t}, \boldsymbol{D} \cdot \boldsymbol{n}$ are continuous at the interface between two cells and we will denote by

- $\varepsilon_p, \mu_p, \rho_p, H_p$ and $B_p = \mu_p H_p$ approximations of ε, μ, ρ, B and H at the point ξ_p in P_p,
- ρ_d, H_d approximations of ρ, H at the point $\boldsymbol{x}_d$ in Π_d and $B_{dp} = \mu_p H_d$ an approximation of B in $\Pi_d \cap P_p$,
- H_s an approximation of H at the point ξ_s,
- α_s, β_s approximations of α, β at the (boundary) point ξ_s,
- α_d, β_d approximations of α, β at the (boundary) point $\boldsymbol{x}_d$,

- $\boldsymbol{j}_s$ an approximation of $\boldsymbol{j}$ in Q_s,
- $\boldsymbol{j}_d \cdot \boldsymbol{n}_d = \frac{1}{|\partial \Pi_d \cap \partial\Omega|} \int_{\partial \Pi_d \cap \partial\Omega} \boldsymbol{j} \cdot \boldsymbol{n}$ (for $\boldsymbol{x}_d \in \partial\Omega$),
- $\boldsymbol{E}_{sp}$ and $\boldsymbol{E}_{sq}$ approximations of $\boldsymbol{E}$ in Q_{sp} and Q_{sq} such that

$$\boldsymbol{E}_{sp} \cdot \boldsymbol{t}_s = \boldsymbol{E}_{sq} \cdot \boldsymbol{t}_s \overset{\text{def}}{=} \boldsymbol{E}_s \cdot \boldsymbol{t}_s,$$

- $\boldsymbol{D}_{sp} = \varepsilon_p \boldsymbol{E}_{sp}$ and $\boldsymbol{D}_{sq} = \varepsilon_q \boldsymbol{E}_{sq}$ approximations of $\boldsymbol{D}$ in Q_{sp} and Q_{sq} such that

$$\boldsymbol{D}_{sp} \cdot \boldsymbol{n}_s = \boldsymbol{D}_{sq} \cdot \boldsymbol{n}_s \overset{\text{def}}{=} \boldsymbol{D}_s \cdot \boldsymbol{n}_s,$$

- $\boldsymbol{E}_d \cdot \boldsymbol{t}_d \overset{\text{def}}{=} \frac{1}{|\partial \Pi_d \cap \partial\Omega|} \int_{\partial \Pi_d \cap \partial\Omega} \boldsymbol{E} \cdot \boldsymbol{t}$ (for $\boldsymbol{x}_d \in \partial\Omega$),
- $\boldsymbol{D}_d \cdot \boldsymbol{n}_d \overset{\text{def}}{=} \frac{1}{|\partial \Pi_d \cap \partial\Omega|} \int_{\partial \Pi_d \cap \partial\Omega} \boldsymbol{D} \cdot \boldsymbol{n}$ (for $\boldsymbol{x}_d \in \partial\Omega$).

Furthermore we will denote by

- $\varepsilon_s = \frac{\varepsilon_p c_{sp} |\Sigma_{sp}| + \varepsilon_q c_{sq} |\Sigma_{sq}|}{c_{sp} |\Sigma_{sp}| + c_{sq} |\Sigma_{sq}|}$ a first approximation of ε in Q_s,
- $\bar{\varepsilon}_s = \frac{\varepsilon_p \varepsilon_q (c_{sp} |\Sigma_{sp}| + c_{sq} |\Sigma_{sq}|)}{\varepsilon_q c_{sp} |\Sigma_{sp}| + \varepsilon_p c_{sq} |\Sigma_{sq}|}$ a second approximation of ε in Q_s,
- $\mu_d = \sum_{P_p} \mu_p \frac{\|\Pi_d \cap P_p\|}{\|\Pi_d\|}$ an approximation of μ at the point $\boldsymbol{x}_d$.

The degrees of freedom of our method will be H_p, H_d, H_s (if $\xi_s \in \partial\Omega$), $\boldsymbol{E}_s \cdot \boldsymbol{t}_s, \boldsymbol{D}_s \cdot \boldsymbol{n}_s, \boldsymbol{E}_d \cdot \boldsymbol{t}_d$ (if $\boldsymbol{x}_d \in \partial\Omega$) and $\boldsymbol{D}_d \cdot \boldsymbol{n}_d$ (if $\boldsymbol{x}_d \in \partial\Omega$).

4.1. Space-discretization: the finite volume method

For example consider the system (5). As proposed in [59] let us perform the following operations

- integrate the first (Faraday) equation over each primal polygon P_p and over each sub-polygon $\Pi_d \cap P_p$,
- take the flux of the second (Ampere–Maxwell) equation over each primal (dual) side(s) $S_s(\Sigma_{sp}, \Sigma_{sq})$ and over each (dual) boundary side $\partial\Pi_d \cap \partial\Omega$.

Thereby we obtain, after using standard vector identities:

$$\begin{cases} \frac{\partial}{\partial t}\left(\int\int_{P_p} B\right) + \int_{\partial P_p} \boldsymbol{E} \cdot \boldsymbol{t} = 0, \\ \frac{\partial}{\partial t}\left(\int\int_{\Pi_d \cap P_p} B\right) + \int_{\Pi_d \cap \partial P_p} \boldsymbol{E} \cdot \boldsymbol{t} - \int_{\partial \Pi_d \cap P_p} \boldsymbol{E} \cdot \boldsymbol{\tau} = 0, \\ \frac{\partial}{\partial t}\left(\int_{S_s} \boldsymbol{D} \cdot \boldsymbol{n}_s\right) - \int_{S_s} \nabla H \cdot \boldsymbol{t}_s = -\int_{S_s} \boldsymbol{j} \cdot \boldsymbol{n}_s, \\ \frac{\partial}{\partial t}\left(\int_{\Sigma_{sp}} \boldsymbol{D}.\boldsymbol{v}_{sp}\right) + \int_{\Sigma_{sp}} \nabla H \cdot \boldsymbol{\tau}_{sp} = -\int_{\Sigma_{sp}} \boldsymbol{j} \cdot \boldsymbol{v}_{sp}, \\ \frac{\partial}{\partial t}\left(\int_{\Sigma_{sq}} \boldsymbol{D}.\boldsymbol{v}_{sq}\right) + \int_{\Sigma_{sq}} \nabla H \cdot \boldsymbol{\tau}_{sq} = -\int_{\Sigma_{sq}} \boldsymbol{j} \cdot \boldsymbol{v}_{sq}, \\ \frac{\partial}{\partial t}\left(\int_{\partial \Pi_d \cap \partial\Omega} \boldsymbol{D} \cdot \boldsymbol{n}\right) - \int_{\partial \Pi_d \cap \partial\Omega} \nabla H \cdot \boldsymbol{t} = -\int_{\partial \Pi_d \cap \partial\Omega} \boldsymbol{j} \cdot \boldsymbol{n}. \end{cases} \tag{8}$$

Using the approximations introduced at the beginning of this section provides

$$\begin{cases} \|P_p\| \frac{\partial B_p}{\partial t} + \sum_{S_s \in \partial P_p} |S_s| \boldsymbol{E}_s \cdot \boldsymbol{t}_s = 0, \\ \|\Pi_d \cap P_p\| \frac{\partial B_{dp}}{\partial t} + \int_{\Pi_d \cap \partial P_p} \boldsymbol{E} \cdot \boldsymbol{t} - \int_{\partial \Pi_d \cap P_p} \boldsymbol{E} \cdot \boldsymbol{\tau} = 0, \\ |S_s| \frac{\partial}{\partial t}(\boldsymbol{D}_s \cdot \boldsymbol{n}_s) - H_e + H_d = -|S_s| \boldsymbol{j}_s \cdot \boldsymbol{n}_s, \\ |\Sigma_{sp}| \frac{\partial}{\partial t}(\boldsymbol{D}_{sp} \cdot \boldsymbol{v}_{sp}) - H_p + H_s = -|\Sigma_{sp}| \boldsymbol{j}_s \cdot \boldsymbol{v}_{sp}, \\ |\Sigma_{sq}| \frac{\partial}{\partial t}(\boldsymbol{D}_{sq} \cdot \boldsymbol{v}_{sq}) - H_s + H_q = -|\Sigma_{sq}| \boldsymbol{j}_s \cdot \boldsymbol{v}_{sq}, \\ |\partial \Pi_d \cap \partial\Omega| \frac{\partial}{\partial t}(\boldsymbol{D}_d \cdot \boldsymbol{n}_d) - H_u + H_r = -|\partial \Pi_d \cap \partial\Omega| \boldsymbol{j}_d \cdot \boldsymbol{n}_d. \end{cases} \tag{9}$$

By adding the second equation over all the primal polygons P_p such that $P_p \cap \Pi_d \neq \emptyset$ we obtain

$$\sum_{P_p} \|\Pi_d \cap P_p\| \frac{\partial B_{dp}}{\partial t} - \sum_{\Sigma_{sp}, \Sigma_{sq} \in \partial \Pi_d} (|\Sigma_{sp}| \boldsymbol{E}_{sp} \cdot \boldsymbol{\tau}_{sp} + |\Sigma_{sq}| \boldsymbol{E}_{sq} \cdot \boldsymbol{\tau}_{sq}) + |\partial \Pi_d \cap \partial\Omega| \boldsymbol{E}_d \cdot \boldsymbol{t}_d = 0.$$

Since, by definition, $B_{dp} = \mu_p H_d$ and $\mu_d \|\Pi_d\| = \sum_{P_p} \mu_p \|\Pi_d \cap P_p\|$ we obtain, thanks to (4)

$$\mu_d \|\Pi_d\| \frac{\partial H_d}{\partial t} - \sum_{\Sigma_s \in \partial \Pi_d} |\Sigma_s| \left(\frac{1}{\bar{\varepsilon}_s} c_s \boldsymbol{D}_s \cdot \boldsymbol{n}_s + s_s \boldsymbol{E}_s \cdot \boldsymbol{t}_s\right) + |\partial \Pi_d \cap \partial\Omega| \boldsymbol{E}_d \cdot \boldsymbol{t}_d = 0.$$

The discretization of the boundary condition on $\partial\Pi_d \cap \partial\Omega$ provides

$$\alpha_d \boldsymbol{E}_d \cdot \boldsymbol{t}_d - \beta_d H_d \simeq g_d.$$

If $\alpha_d = 0$ and $\beta_d \neq 0$ then

$$H_d = -\frac{g_d}{\beta_d}.$$

If $\alpha_d \neq 0$ then

$$\boldsymbol{E}_d \cdot \boldsymbol{t}_d = \frac{\beta_d}{\alpha_d} H_d + \frac{g_d}{\alpha_d}$$

and we obtain

$$\mu_d \|\Pi_d\| \frac{\partial H_d}{\partial t} + |\partial\Pi_d \cap \partial\Omega| \frac{\beta_d}{\alpha_d} H_d - \sum_{\Sigma_s \in \partial\Pi_d} |\Sigma_s| \left(\frac{1}{\bar{\varepsilon}_s} c_s \boldsymbol{D}_s \cdot \boldsymbol{n}_s + s_s \boldsymbol{E}_s \cdot \boldsymbol{t}_s \right) = -|\partial\Pi_d \cap \partial\Omega| \frac{g_d}{\alpha_d}.$$

Since $\boldsymbol{D} = \varepsilon \boldsymbol{E}$, the discretized Maxwell–Ampere laws, that is the third, fourth and fifth equations of system (9), can be rewritten as

$$\begin{cases} \varepsilon_p |S_s| \frac{\partial}{\partial t} (\boldsymbol{E}_{sp} \cdot \boldsymbol{n}_s) - H_e + H_d = -|S_s| \boldsymbol{j}_s \cdot \boldsymbol{n}_s & (\text{in } P_p), \\ \varepsilon_q |S_s| \frac{\partial}{\partial t} (\boldsymbol{E}_{sq} \cdot \boldsymbol{n}_s) - H_e + H_d = -|S_s| \boldsymbol{j}_s \cdot \boldsymbol{n}_s & (\text{in } P_q \text{ if } S_s \notin \partial\Omega), \\ \varepsilon_p |\Sigma_{sp}| \frac{\partial}{\partial t} (\boldsymbol{E}_{sp} \cdot \boldsymbol{v}_{sp}) - H_p + H_s = -|\Sigma_{sp}| \boldsymbol{j}_s \cdot \boldsymbol{v}_{sp} & (\text{in } P_p), \\ \varepsilon_q |\Sigma_{sq}| \frac{\partial}{\partial t} (\boldsymbol{E}_{sq} \cdot \boldsymbol{v}_{sq}) - H_s + H_q = -|\Sigma_{sq}| \boldsymbol{j}_s \cdot \boldsymbol{v}_{sq} & (\text{in } P_q \text{ if } S_s \notin \partial\Omega). \end{cases} \tag{10}$$

Thanks to (3) the last two equations of (10) read

$$\varepsilon_p c_{sp} |\Sigma_{sp}| \frac{\partial}{\partial t} (\boldsymbol{E}_s \cdot \boldsymbol{t}_s) - \varepsilon_p s_{sp} |\Sigma_{sp}| \frac{\partial}{\partial t} (\boldsymbol{E}_{sp} \cdot \boldsymbol{n}_s) - H_p + H_s = -|\Sigma_{sp}| \boldsymbol{j}_s \cdot \boldsymbol{v}_{sp},$$
$$\varepsilon_q c_{sq} |\Sigma_{sq}| \frac{\partial}{\partial t} (\boldsymbol{E}_s \cdot \boldsymbol{t}_s) - \varepsilon_q s_{sq} |\Sigma_{sq}| \frac{\partial}{\partial t} (\boldsymbol{E}_{sq} \cdot \boldsymbol{n}_s) - H_s + H_q = -|\Sigma_{sq}| \boldsymbol{j}_s \cdot \boldsymbol{v}_{sq}.$$

Then using the first two equations of (10) results in

$$\begin{cases} \varepsilon_p c_{sp} |\Sigma_{sp}| \frac{\partial}{\partial t} (\boldsymbol{E}_s \cdot \boldsymbol{t}_s) - s_{sp} \frac{|\Sigma_{sp}|}{|S_s|} (H_e - H_d) - H_p + H_s = -c_{sp} |\Sigma_{sp}| \boldsymbol{j}_s \cdot \boldsymbol{t}_s, \\ \varepsilon_q c_{sq} |\Sigma_{sq}| \frac{\partial}{\partial t} (\boldsymbol{E}_s \cdot \boldsymbol{t}_s) - s_{sq} \frac{|\Sigma_{sq}|}{|S_s|} (H_e - H_d) - H_s + H_q = -c_{sq} |\Sigma_{sq}| \boldsymbol{j}_s \cdot \boldsymbol{t}_s. \end{cases} \tag{11}$$

By adding these equations we obtain, thanks to (2)

$$\varepsilon_s \|Q_s\| \frac{\partial}{\partial t} (\boldsymbol{E}_s \cdot \boldsymbol{t}_s) + \frac{1}{2} |S_s| (H_q - H_p) - \frac{1}{2} s_s |\Sigma_s| (H_e - H_d) = -\|Q_s\| \boldsymbol{j}_s \cdot \boldsymbol{t}_s.$$

For a boundary primal side S_s for which $H_q = H_s$ we would obtain

$$\varepsilon_s \|Q_s\| \frac{\partial}{\partial t} (\boldsymbol{E}_s \cdot \boldsymbol{t}_s) + \frac{1}{2} |S_s| (H_s - H_p) - \frac{1}{2} s_s |\Sigma_s| (H_e - H_d) = -\|Q_s\| \boldsymbol{j}_s \cdot \boldsymbol{t}_s.$$

The discretization of the boundary condition on the side S_s provides

$$\alpha_s \boldsymbol{E}_s \cdot \boldsymbol{t}_s - \beta_s H_s = g_s.$$

If $\alpha_s \neq 0$ and $\beta_s = 0$ then

$$\boldsymbol{E}_s \cdot \boldsymbol{t}_s = \frac{g_s}{\alpha_s}.$$

If $\beta_s \neq 0$ then

$$H_s = \frac{\alpha_s}{\beta_s} \boldsymbol{E}_s \cdot \boldsymbol{t}_s - \frac{g_s}{\beta_s}$$

and we obtain

$$\varepsilon_s \|Q_s\| \frac{\partial}{\partial t} (\boldsymbol{E}_s \cdot \boldsymbol{t}_s) + \frac{1}{2} |S_s| \frac{\alpha_s}{\beta_s} \boldsymbol{E}_s \cdot \boldsymbol{t}_s - \frac{1}{2} |S_s| H_p - \frac{1}{2} s_s |\Sigma_s| (H_e - H_d) = -\|Q_s\| \boldsymbol{j}_s \cdot \boldsymbol{t}_s + \frac{1}{2} |S_s| \frac{g_s}{\beta_s}.$$

At the end, the system (9) results in

$$
\begin{cases}
\mu_{\mathrm{p}}\|P_{\mathrm{p}}\|\frac{\partial H_{\mathrm{p}}}{\partial t}+\sum\limits_{S_{\mathrm{s}}\in\partial P_{\mathrm{p}}}|S_{\mathrm{s}}|\boldsymbol{E}_{\mathrm{s}}\cdot\boldsymbol{t}_{\mathrm{s}}=0,\\
\mu_{\mathrm{d}}\|\Pi_{\mathrm{d}}\|\frac{\partial H_{\mathrm{d}}}{\partial t}-\sum\limits_{\Sigma_{\mathrm{s}}\in\partial\Pi_{\mathrm{d}}}|\Sigma_{\mathrm{s}}|\left(\frac{1}{\varepsilon_{\mathrm{s}}}c_{\mathrm{s}}\boldsymbol{D}_{\mathrm{s}}\cdot\boldsymbol{n}_{\mathrm{s}}+s_{\mathrm{s}}\boldsymbol{E}_{\mathrm{s}}\cdot\boldsymbol{t}_{\mathrm{s}}\right)=0\quad(\boldsymbol{x}_{\mathrm{d}}\notin\partial\Omega),\\
H_{\mathrm{d}}=-\frac{g_{\mathrm{d}}}{\beta_{\mathrm{d}}}\quad(\boldsymbol{x}_{\mathrm{d}}\in\partial\Omega,\alpha_{\mathrm{d}}=0),\\
\mu_{\mathrm{d}}\|\Pi_{\mathrm{d}}\|\frac{\partial H_{\mathrm{d}}}{\partial t}+|\partial\Pi_{\mathrm{d}}\cap\partial\Omega|\frac{\beta_{\mathrm{d}}}{\alpha_{\mathrm{d}}}H_{\mathrm{d}}-\sum\limits_{\Sigma_{\mathrm{s}}\in\partial\Pi_{\mathrm{d}}}|\Sigma_{\mathrm{s}}|\left(\frac{1}{\varepsilon_{\mathrm{s}}}c_{\mathrm{s}}\boldsymbol{D}_{\mathrm{s}}\cdot\boldsymbol{n}_{\mathrm{s}}+s_{\mathrm{s}}\boldsymbol{E}_{\mathrm{s}}\cdot\boldsymbol{t}_{\mathrm{s}}\right)=-|\partial\Pi_{\mathrm{d}}\cap\partial\Omega|\frac{g_{\mathrm{d}}}{\alpha_{\mathrm{d}}}\\
\quad(\boldsymbol{x}_{\mathrm{d}}\in\partial\Omega,\alpha_{\mathrm{d}}\neq0),\\
\|Q_{\mathrm{s}}\|\frac{\partial}{\partial t}(\boldsymbol{D}_{\mathrm{s}}\cdot\boldsymbol{n}_{\mathrm{s}})\quad-\frac{1}{2}c_{\mathrm{s}}|\Sigma_{\mathrm{s}}|(H_e-H_{\mathrm{d}})=-\|Q_{\mathrm{s}}\|\boldsymbol{j}_{\mathrm{s}}\cdot\boldsymbol{n}_{\mathrm{s}},\\
|\partial\Pi_{\mathrm{d}}\cap\partial\Omega|\frac{\partial}{\partial t}(\boldsymbol{D}_{\mathrm{d}}\cdot\boldsymbol{n}_{\mathrm{d}})-H_u+H_r=-|\partial\Pi_{\mathrm{d}}\cap\partial\Omega|\boldsymbol{j}_{\mathrm{d}}\cdot\boldsymbol{n}_{\mathrm{d}}\quad(\boldsymbol{x}_{\mathrm{d}}\in\partial\Omega),\\
\varepsilon_{\mathrm{s}}\|Q_{\mathrm{s}}\|\frac{\partial}{\partial t}(\boldsymbol{E}_{\mathrm{s}}\cdot\boldsymbol{t}_{\mathrm{s}})+\frac{1}{2}|S_{\mathrm{s}}|(H_{\mathrm{q}}-H_{\mathrm{p}})-\frac{1}{2}s_{\mathrm{s}}|\Sigma_{\mathrm{s}}|(H_e-H_{\mathrm{d}})=-\|Q_{\mathrm{s}}\|\boldsymbol{j}_{\mathrm{s}}\cdot\boldsymbol{t}_{\mathrm{s}}\quad(S_{\mathrm{s}}\notin\partial\Omega),\\
\boldsymbol{E}_{\mathrm{s}}\cdot\boldsymbol{t}_{\mathrm{s}}=\frac{g_{\mathrm{s}}}{\alpha_{\mathrm{s}}}\quad(S_{\mathrm{s}}\in\partial\Omega,\beta_{\mathrm{s}}=0),\\
\varepsilon_{\mathrm{s}}\|Q_{\mathrm{s}}\|\frac{\partial}{\partial t}(\boldsymbol{E}_{\mathrm{s}}\cdot\boldsymbol{t}_{\mathrm{s}})+\frac{1}{2}|S_{\mathrm{s}}|\frac{\alpha_{\mathrm{s}}}{\beta_{\mathrm{s}}}\boldsymbol{E}_{\mathrm{s}}\cdot\boldsymbol{t}_{\mathrm{s}}-\frac{1}{2}|S_{\mathrm{s}}|H_{\mathrm{p}}-\frac{1}{2}s_{\mathrm{s}}|\Sigma_{\mathrm{s}}|(H_e-H_{\mathrm{d}})=-\|Q_{\mathrm{s}}\|\boldsymbol{j}_{\mathrm{s}}\cdot\boldsymbol{t}_{\mathrm{s}}+\frac{1}{2}|S_{\mathrm{s}}|\frac{g_{\mathrm{s}}}{\beta_{\mathrm{s}}}\\
\quad(S_{\mathrm{s}}\in\partial\Omega,\beta_{\mathrm{s}}\neq0).
\end{cases}
\tag{12}
$$

4.2. Time-discretization: the leap-frog scheme

Consider (12). The leap-frog scheme provides the following full discretization of the Maxwell equation (5)

$$
\begin{cases}
\mu_{\mathrm{p}}\|P_{\mathrm{p}}\|H_{\mathrm{p}}^{n+1}=\mu_{\mathrm{p}}\|P_{\mathrm{p}}\|H_{\mathrm{p}}^{n}-\Delta t\sum\limits_{S_{\mathrm{s}}\in\partial P_{\mathrm{p}}}|S_{\mathrm{s}}|\boldsymbol{E}_{\mathrm{s}}^{n+\frac12}\cdot\boldsymbol{t}_{\mathrm{s}}=0,\\
\mu_{\mathrm{d}}\|\Pi_{\mathrm{d}}\|H_{\mathrm{d}}^{n+1}=\mu_{\mathrm{d}}\|\Pi_{\mathrm{d}}\|H_{\mathrm{d}}^{n}+\Delta t\sum\limits_{\Sigma_{\mathrm{s}}\in\partial\Pi_{\mathrm{d}}}|\Sigma_{\mathrm{s}}|\left(\frac{1}{\varepsilon_{\mathrm{s}}}c_{\mathrm{s}}\boldsymbol{D}_{\mathrm{s}}^{n+\frac12}\cdot\boldsymbol{n}_{\mathrm{s}}+s_{\mathrm{s}}\boldsymbol{E}_{\mathrm{s}}^{n+\frac12}.\boldsymbol{t}_{\mathrm{s}}\right)\quad(\boldsymbol{x}_{\mathrm{d}}\notin\partial\Omega),\\
H_{\mathrm{d}}^{n+1}=-\frac{g_{\mathrm{d}}^{n+1}}{\beta_{\mathrm{d}}}\quad(\boldsymbol{x}_{\mathrm{d}}\in\partial\Omega,\ \alpha_{\mathrm{d}}=0),\\
\left(\mu_{\mathrm{d}}\|\Pi_{\mathrm{d}}\|+\frac{\Delta t}{2}|\partial\Pi_{\mathrm{d}}\cap\partial\Omega|\right)\frac{\beta_{\mathrm{d}}}{\alpha_{\mathrm{d}}}H_{\mathrm{d}}^{n+1}=\left(\mu_{\mathrm{d}}\|\Pi_{\mathrm{d}}\|-\frac{\Delta t}{2}|\partial\Pi_{\mathrm{d}}\cap\partial\Omega|\right)\frac{\beta_{\mathrm{d}}}{\alpha_{\mathrm{d}}}H_{\mathrm{d}}^{n}\\
\quad+\Delta t\sum\limits_{\Sigma_{\mathrm{s}}\in\partial\Pi_{\mathrm{d}}}|\Sigma_{\mathrm{s}}|\left(\frac{1}{\varepsilon_{\mathrm{s}}}c_{\mathrm{s}}\boldsymbol{D}_{\mathrm{s}}^{n+\frac12}\cdot\boldsymbol{n}_{\mathrm{s}}+s_{\mathrm{s}}\boldsymbol{E}_{\mathrm{s}}^{n+\frac12}.\boldsymbol{t}_{\mathrm{s}}\right)-\Delta t|\partial\Pi_{\mathrm{d}}\cap\partial\Omega|\frac{g_{\mathrm{d}}^{n+\frac12}}{\alpha_{\mathrm{d}}}\\
\quad(\boldsymbol{x}_{\mathrm{d}}\in\partial\Omega,\alpha_{\mathrm{d}}\neq0),\\
|\partial\Pi_{\mathrm{d}}\cap\partial\Omega|\boldsymbol{D}_{\mathrm{d}}^{n+\frac12}\cdot\boldsymbol{n}_{\mathrm{d}}=|\partial\Pi_{\mathrm{d}}\cap\partial\Omega|\boldsymbol{D}_{\mathrm{d}}^{n-\frac12}\cdot\boldsymbol{n}_{\mathrm{d}}-\Delta t(H_u^n-H_r^n)-|\partial\Pi_{\mathrm{d}}\cap\partial\Omega|\boldsymbol{j}_{\mathrm{d}}^{n}\cdot\boldsymbol{n}_{\mathrm{d}}\quad(\boldsymbol{x}_{\mathrm{d}}\in\partial\Omega),\\
\|Q_{\mathrm{s}}\|\boldsymbol{D}_{\mathrm{s}}^{n+\frac12}\cdot\boldsymbol{n}_{\mathrm{s}}=\|Q_{\mathrm{s}}\|\boldsymbol{D}_{\mathrm{s}}^{n-\frac12}\cdot\boldsymbol{n}_{\mathrm{s}}+\frac{1}{2}\Delta tc_{\mathrm{s}}|\Sigma_{\mathrm{s}}|(H_e^n-H_{\mathrm{d}}^n)-\Delta t\|Q_{\mathrm{s}}\|\boldsymbol{j}_{\mathrm{s}}^{n}\cdot\boldsymbol{n}_{\mathrm{s}},\\
\varepsilon_{\mathrm{s}}\|Q_{\mathrm{s}}\|\boldsymbol{E}_{\mathrm{s}}^{n+\frac12}\cdot\boldsymbol{t}_{\mathrm{s}}=\varepsilon_{\mathrm{s}}\|Q_{\mathrm{s}}\|\boldsymbol{E}_{\mathrm{s}}^{n-\frac12}\cdot\boldsymbol{t}_{\mathrm{s}}-\frac{1}{2}\Delta t|S_{\mathrm{s}}|(H_{\mathrm{q}}^n-H_{\mathrm{p}}^n)+\frac{1}{2}\Delta ts_{\mathrm{s}}|\Sigma_{\mathrm{s}}|(H_e^n-H_{\mathrm{d}}^n)-\Delta t\|Q_{\mathrm{s}}\|\boldsymbol{j}_{\mathrm{s}}^{n}\cdot\boldsymbol{t}_{\mathrm{s}}\\
\quad(S_{\mathrm{s}}\notin\partial\Omega),\\
\boldsymbol{E}_{\mathrm{s}}^{n+\frac12}\cdot\boldsymbol{t}_{\mathrm{s}}=\frac{g_{\mathrm{s}}^{n+\frac12}}{\alpha_{\mathrm{s}}}\quad(S_{\mathrm{s}}\in\partial\Omega,\beta_{\mathrm{s}}=0),\\
\left(\varepsilon_{\mathrm{s}}\|Q_{\mathrm{s}}\|+\frac{\Delta t}{4}|S_{\mathrm{s}}|\frac{\alpha_{\mathrm{s}}}{\beta_{\mathrm{s}}}\right)\boldsymbol{E}_{\mathrm{s}}^{n+\frac12}.\boldsymbol{t}_{\mathrm{s}}=\left(\varepsilon_{\mathrm{s}}\|Q_{\mathrm{s}}\|-\frac{\Delta t}{4}|S_{\mathrm{s}}|\frac{\alpha_{\mathrm{s}}}{\beta_{\mathrm{s}}}\right)\boldsymbol{E}_{\mathrm{s}}^{n-\frac12}\cdot\boldsymbol{t}_{\mathrm{s}}+\frac{1}{2}\Delta t|S_{\mathrm{s}}|H_{\mathrm{p}}^n+\frac{1}{2}\Delta ts_{\mathrm{s}}|\Sigma_{\mathrm{s}}|(H_e^n-H_{\mathrm{d}}^n)\\
\quad-\Delta t\|Q_{\mathrm{s}}\|\boldsymbol{j}_{\mathrm{s}}^{n}\cdot\boldsymbol{t}_{\mathrm{s}}+\Delta t|S_{\mathrm{s}}|\frac{g_{\mathrm{s}}^{n}}{\beta_{\mathrm{s}}}\quad(S_{\mathrm{s}}\in\partial\Omega,\beta_{\mathrm{s}}\neq0).
\end{cases}
\tag{13}
$$

4.2.1. Gauss' law

As it has been noticed for the initial continuous system (5), and as it could be proved for the space-discretized system (12), one can check that in the fully discretized system (13), the discretized Gauss laws are satisfied at any time, provided they are satisfied at the initial time and if both following discretized charge conservation laws hold (for the proof, see Section 5.4):

$$
\begin{cases}
\|P_{\mathrm{p}}\|\rho_{\mathrm{p}}^{n+\frac12}=\|P_{\mathrm{p}}\|\rho_{\mathrm{p}}^{n-\frac12}-\Delta t\sum\limits_{S_{\mathrm{s}}\in\partial P_{\mathrm{p}}}|S_{\mathrm{s}}|\boldsymbol{j}_{\mathrm{s}}^{n}\cdot\boldsymbol{n}_{\mathrm{s}},\\
\|\Pi_{\mathrm{d}}\|\rho_{\mathrm{d}}^{n+\frac12}=\|\Pi_{\mathrm{d}}\|\rho_{\mathrm{d}}^{n-\frac12}-\Delta t\sum\limits_{\Sigma_{\mathrm{sp}},\Sigma_{\mathrm{sq}}\in\partial\Pi_{\mathrm{d}}}(|\Sigma_{\mathrm{sp}}|\boldsymbol{j}_{\mathrm{s}}^{n}\cdot\boldsymbol{v}_{\mathrm{sp}}+|\Sigma_{\mathrm{sq}}|\boldsymbol{j}_{\mathrm{s}}^{n}.\boldsymbol{v}_{\mathrm{sq}})-\Delta t|\partial\Pi_{\mathrm{d}}\cap\partial\Omega|\boldsymbol{j}_{\mathrm{d}}^{n}\cdot\boldsymbol{n}_{\mathrm{d}}.
\end{cases}
$$

For satisfying these equations, note that we can choose the following approximations of the continuous charge and current densities

$$
\rho_{\mathrm{p}}^{n+\frac12}=\frac{1}{\|P_{\mathrm{p}}\|}\int_{P_{\mathrm{p}}}\rho^{n+\frac12},\quad\rho_{\mathrm{d}}^{n+\frac12}=\frac{1}{\|\Pi_{\mathrm{d}}\|}\int_{\Pi_{\mathrm{d}}}\rho^{n+\frac12}
$$

and

$$\boldsymbol{j}_{\mathrm{s}}^{n}\cdot\boldsymbol{n}_{\mathrm{s}}=\frac{1}{\Delta t}\frac{1}{|S_{\mathrm{s}}|}\int_{n\Delta t-\frac{\Delta t}{2}}^{n\Delta t+\frac{\Delta t}{2}}\int_{S_{\mathrm{s}}}\boldsymbol{j}\cdot\boldsymbol{n}_{\mathrm{s}},$$

$$\boldsymbol{j}_{\mathrm{s}}^{n}.(|\Sigma_{\mathrm{sp}}|\boldsymbol{v}_{\mathrm{sp}}+|\Sigma_{\mathrm{sq}}|\boldsymbol{v}_{\mathrm{sq}})=\frac{1}{\Delta t}\int_{n\Delta t-\frac{\Delta t}{2}}^{n\Delta t+\frac{\Delta t}{2}}\int_{\Sigma_{\mathrm{sp}}}\boldsymbol{j}\cdot\boldsymbol{v}_{\mathrm{sp}}+\frac{1}{\Delta t}\int_{n\Delta t-\frac{\Delta t}{2}}^{n\Delta t+\frac{\Delta t}{2}}\int_{\Sigma_{\mathrm{sq}}}\boldsymbol{j}\cdot\boldsymbol{v}_{\mathrm{sq}},$$

$$\boldsymbol{j}_{\mathrm{d}}^{n}\cdot\boldsymbol{n}_{\mathrm{d}}=\frac{1}{\Delta t}\frac{1}{|\partial\Pi_{\mathrm{d}}\cap\partial\Omega|}\int_{n\Delta t-\frac{\Delta t}{2}}^{n\Delta t+\frac{\Delta t}{2}}\int_{\partial\Pi_{\mathrm{d}}\cap\partial\Omega}\boldsymbol{j}\cdot\boldsymbol{n}.$$

4.2.2. Energy law and stability

For the sake of simplicity, consider a homogeneous media for which: $\varepsilon_{\mathrm{p}}=\varepsilon_{\mathrm{q}}=\varepsilon$ and $\mu_{\mathrm{p}}=\mu_{\mathrm{q}}=\mu$, and suppose that $\boldsymbol{E}_{\mathrm{s}}\cdot\boldsymbol{t}_{\mathrm{s}}=0$ for all boundary sides (perfect conductor boundary condition). The following equality holds (see Section 5.4 for the proof)

$$\begin{aligned}&\frac{1}{\Delta t}\frac{\mu}{4}\left[\left(\sum_{P_{\mathrm{p}}}\|P_{\mathrm{p}}\|(H_{\mathrm{p}}^{n+1})^2+\sum_{\Pi_{\mathrm{d}}}\|\Pi_{\mathrm{d}}\|(H_{\mathrm{d}}^{n+1})^2\right)-\left(\sum_{P_{\mathrm{p}}}\|P_{\mathrm{p}}\|(H_{\mathrm{p}}^{n})^2+\sum_{\Pi_{\mathrm{d}}}\|\Pi_{\mathrm{d}}\|(H_{\mathrm{d}}^{n})^2\right)\right]\\&+\frac{1}{\Delta t}\frac{\varepsilon}{2}\left(\sum_{Q_{\mathrm{s}}}\|Q_{\mathrm{s}}\|\boldsymbol{E}_{\mathrm{s}}^{n+\frac{3}{2}}.\boldsymbol{E}_{\mathrm{s}}^{n+\frac{1}{2}}-\sum_{Q_{\mathrm{s}}}\|Q_{\mathrm{s}}\|\boldsymbol{E}_{\mathrm{s}}^{n+\frac{1}{2}}\cdot\boldsymbol{E}_{\mathrm{s}}^{n-\frac{1}{2}}\right)=-\sum_{S_{\mathrm{s}}}\|Q_{\mathrm{s}}\|\frac{(\boldsymbol{j}_{\mathrm{s}}^{n+1}+\boldsymbol{j}_{\mathrm{s}}^{n})}{2}\cdot\boldsymbol{E}_{\mathrm{s}}^{n+\frac{1}{2}}.\end{aligned}\tag{14}$$

In this expression one recognizes an approximation of the integrated energy equation (7).

By using such an energy approach we find the following stability condition (see the Appendix for the proof):

$$c\Delta t\leqslant\sqrt{2}\min_{Q_{\mathrm{s}}}\left(|S_{\mathrm{s}}|\min\left\{\frac{r_{\mathrm{sp}}^2}{c_{\mathrm{sp}}}\left[\left(s_{\mathrm{sp}}^2+\frac{c_{\mathrm{sp}}^2}{r_{\mathrm{sp}}^2}\right)^{\frac{1}{2}}-s_{\mathrm{sp}}\right],\frac{r_{\mathrm{sq}}^2}{c_{\mathrm{sq}}}\left[\left(s_{\mathrm{sq}}^2+\frac{c_{\mathrm{sq}}^2}{r_{\mathrm{sq}}^2}\right)^{\frac{1}{2}}-s_{\mathrm{sq}}\right]\right\}\right)\tag{15}$$

with

$$r_{\mathrm{sp}}=\min\left(c_{\mathrm{sp}}\frac{|\Sigma_{\mathrm{sp}}|}{|S_{\mathrm{s}}|},\frac{1}{2}\right),\quad r_{\mathrm{sq}}=\min\left(c_{\mathrm{sq}}\frac{|\Sigma_{\mathrm{sq}}|}{|S_{\mathrm{s}}|},\frac{1}{2}\right).$$

For arbitrary cells such that, for all $S_{\mathrm{s}}, s_{\mathrm{sp}}=s_{\mathrm{sq}}=0$ and $c_{\mathrm{sp}}=c_{\mathrm{sq}}=1$ (orthogonality of primal and dual edges), we would obtain

$$c\Delta t\leqslant\frac{\sqrt{2}}{2}\min\left(2\min_{S_{\mathrm{s}}}|\Sigma_{\mathrm{sp}}|,2\min_{S_{\mathrm{s}}\notin\partial\Omega}|\Sigma_{\mathrm{sq}}|,\min_{S_{\mathrm{s}}}|S_{\mathrm{s}}|\right).\tag{16}$$

A comparison of such a CFL condition with those of standard schemes is provided in Section 6.

5. An equivalent formulation based on discrete differential operators

As said in the introduction, a recent point of view developed in [51–53] for the discretization of various partial differential equations consists in replacing the continuous differential operators by discrete ones defined on arbitrary meshes thanks to an appropriate choice of discrete scalar and vector fields. We shall show that this formulation is equivalent to that given in Section 4.2 and that it also enables to derive properties of the scheme exposed in Sections 4.2.1 and 4.2.2. For the sake of simplicity, we present this formulation in the case of electromagnetic propagation in the vacuum, although heterogeneous media may also be considered. The notations employed in what follows are the same as those given in Sections 2 and 4.

5.1. Definitions of discrete scalar and vector fields and scalar products

We shall consider here scalar fields defined over both primal and dual cell and on boundary primal sides. A discrete scalar field B is given by its values $(B_{\mathrm{p}},B_{\mathrm{d}},B_{\mathrm{s}})$, respectively, on primal cells P_{p}, dual cells Π_{d}, and boundary sides S_{s}. We define the following discrete scalar product and associated norm on the primal and dual meshes

$$\langle A,B\rangle_{P\Pi}:=\frac{1}{2}\left(\sum_{\mathrm{p}}\|P_{\mathrm{p}}\|A_{\mathrm{p}}B_{\mathrm{p}}+\sum_{\mathrm{d}}\|\Pi_{\mathrm{d}}\|A_{\mathrm{d}}B_{\mathrm{d}}\right)\quad\text{and}\quad|B|_{P\Pi}^2:=\langle B,B\rangle_{P\Pi}.\tag{17}$$

A discrete vector field $\boldsymbol{E}$ is given by its values $(\boldsymbol{E}_{\mathrm{s}},\boldsymbol{E}_{\mathrm{d}})$, respectively, on diamond-cells Q_{s} and boundary dual cells (see Fig. 3). We define the following discrete scalar product and associated norm on a diamond mesh:

$$\langle \boldsymbol{F}, \boldsymbol{E}\rangle_Q := \sum_s \|Q_s\| \boldsymbol{F}_s \cdot \boldsymbol{E}_s \quad \text{and} \quad |\boldsymbol{E}|_Q^2 := \langle \boldsymbol{E}, \boldsymbol{E}\rangle_Q. \tag{18}$$

We also define a discrete scalar product of the traces of B and $\boldsymbol{E}\cdot\mathbf{t}$ on the boundary by

$$\langle B, \boldsymbol{E}\cdot\mathbf{t}\rangle_{\partial\Omega,h} := \frac{1}{2}\left(\sum_{S_s\in\partial\Omega} |S_s| B_s \boldsymbol{E}_s\cdot\mathbf{t}_s + \sum_{\boldsymbol{x}_d\in\partial\Omega} |\partial\Pi_d\cap\partial\Omega| B_d \boldsymbol{E}_d\cdot\boldsymbol{t}_d\right). \tag{19}$$

5.2. Definition of discrete differential operators

In order to discretize Maxwell's equations, we define discrete differential operators which are the discrete counterparts of the continuous operators that appear in Eq. (5). Let $(\boldsymbol{E}_s, \boldsymbol{E}_d)$ be a given vector field defined like explained in Section 5.1. We define its discrete divergence over primal and dual cells by (see Fig. 3 for the notations)

$$(\nabla_h^P\cdot\boldsymbol{E})_p := \frac{1}{\|P_p\|}\sum_{S_s\in\partial P_p} |S_s|\boldsymbol{E}_s\cdot\mathbf{n}_s \tag{20}$$

and by

$$(\nabla_h^\Pi\cdot\boldsymbol{E})_d := \frac{1}{\|\Pi_d\|}\left(\sum_{\Sigma_s\in\partial\Pi_d}(|\Sigma_{sp}|\boldsymbol{E}_s\cdot\boldsymbol{v}_{sp} + |\Sigma_{sq}|\boldsymbol{E}_s\cdot\boldsymbol{v}_{sq}) + |\partial\Pi_d\cap\partial\Omega|\boldsymbol{E}_d\cdot\boldsymbol{n}_d\right). \tag{21}$$

We stress that $\partial\Pi_d\cap\partial\Omega$ is non-empty if and only if $x_d\in\partial\Omega$. Given a continuous vector field $\boldsymbol{E}$, it is quite easy to see that equalities (20) and (21) are the exact mean values of $\nabla\cdot\boldsymbol{E}$ over the primal and dual cells, respectively, provided the discrete field $\boldsymbol{E}_s$ verifies for all Q_s

$$|S_s|\boldsymbol{E}_s\cdot\mathbf{n}_s = \int_{S_s}\boldsymbol{E}(\sigma)\cdot\mathbf{n}_s\,d\sigma, \tag{22}$$

$$\boldsymbol{E}_s\cdot(|\Sigma_{sp}|\boldsymbol{v}_{sp} + |\Sigma_{sq}|\boldsymbol{v}_{sq}) = \int_{\Sigma_{sp}}\boldsymbol{E}(\sigma)\cdot\boldsymbol{v}_{sp}\,d\sigma + \int_{\Sigma_{sq}}\boldsymbol{E}(\sigma)\cdot\boldsymbol{v}_{sq}\,d\sigma \tag{23}$$

and provided $\boldsymbol{E}_d$ verifies for all $\boldsymbol{x}_d\in\partial\Omega$

$$\boldsymbol{E}_d\cdot\boldsymbol{n}_d = \frac{1}{|\partial\Pi_d\cap\partial\Omega|}\int_{\partial\Pi_d\cap\partial\Omega}\boldsymbol{E}\cdot\boldsymbol{n}(\sigma)\,d\sigma. \tag{24}$$

Note that (22) and (23) uniquely defines the vector $\boldsymbol{E}_s$ on each diamond cell Q_s. In the same way, let $(\boldsymbol{E}_s, \boldsymbol{E}_d)$ be a given vector field. We define its discrete (scalar) curl over primal and dual cells by

$$(\nabla_h^P\times\boldsymbol{E})_p := \frac{1}{\|P_p\|}\sum_{S_s\in\partial P_p}|S_s|\boldsymbol{E}_s\cdot\mathbf{t}_s \tag{25}$$

and by

$$(\nabla_h^\Pi\times\boldsymbol{E})_d := \frac{1}{\|\Pi_d\|}\left(-\sum_{\Sigma_s\in\partial\Pi_d}(|\Sigma_{sp}|\boldsymbol{E}_s\cdot\boldsymbol{\tau}_{sp} + |\Sigma_{sq}|\boldsymbol{E}_s\cdot\boldsymbol{\tau}_{sq}) + |\partial\Pi_d\cap\partial\Omega|\boldsymbol{E}_d\cdot\boldsymbol{t}_d\right). \tag{26}$$

Given a continuous vector field $\boldsymbol{E}$, it is quite easy to see that equalities (25) and (26) are the exact mean values of $\nabla\times\boldsymbol{E}$ over the primal and dual cells, respectively, provided $\boldsymbol{E}$ and $(\boldsymbol{E}_s, \boldsymbol{E}_d)$ verify relations analogous to (22), (24), where the various vectors $\mathbf{n}$ and $\boldsymbol{v}$ are changed into their respective associated tangential vectors $\mathbf{t}$ and $\boldsymbol{\tau}$.

Moreover, given a scalar field $B = (B_p, B_d, B_s)$, defined like explained in Section 5.1, we also need the discrete (vector) curl of B, which we define over the diamond-cells of the mesh by

$$(\mathbf{V}_h^Q\times B)_s := \frac{1}{2\|Q_s\|}[(B_e - B_d)(|\Sigma_{sp}|\boldsymbol{\tau}_{sp} + |\Sigma_{sq}|\boldsymbol{\tau}_{sq}) + (B_p - B_q)|S_s|\mathbf{t}_s]. \tag{27}$$

Given a continuous scalar field B which is P_1 over Q_s, it is an easy matter to show that this formula is the exact curl of B provided $B_e = B(\mathbf{x}_e), B_d = B(\mathbf{x}_d), B_p = B(\xi_p)$ and $B_q = B(\xi_q)$. Moreover, we have

$$\int_{S_s}(\mathbf{V}_h^Q\times B)_s\cdot\mathbf{n}_s = B_e - B_d$$

and

$$\int_{\Sigma_{sp}}(\mathbf{V}_h^Q\times B)_s\cdot\boldsymbol{v}_{sp} + \int_{\Sigma_{sq}}(\mathbf{V}_h^Q\times B)_s\cdot\boldsymbol{v}_{sq} = B_p - B_q.$$

If $S_s\in\partial\Omega$, there is a slight modification which reads

$$(\mathbf{V}_h^Q\times B)_s := \frac{1}{2\|Q_s\|}[(B_e - B_d)|\Sigma_{sp}|\boldsymbol{\tau}_{sp} + (B_p - B_s)|S_s|\mathbf{t}_s]. \tag{28}$$

Finally, for boundary points $x_d \in \partial\Omega$, we define the normal component of $(\mathbf{V}_h^Q \times B)_d$ by the following quantity (see Fig. 3 for the notations):

$$|\partial\Pi_d \cap \partial\Omega|(\mathbf{V}_h^Q \times B)_d \cdot \mathbf{n}_d := (B_u - B_r). \tag{29}$$

We note that the boundary scalar product (19) and the definition of the discrete divergence (21) and scalar curl operator (26) for boundary dual cells slightly differ from those given in [51,53]. Indeed, in these references, the values of $\boldsymbol{E}_d$ associated with the boundary nodes $\boldsymbol{x}_d$ were expressed as a linear combination of the values $\boldsymbol{E}_s$ associated with the neighbouring boundary edges, while in this paper the values of $\boldsymbol{E}_d$ are independent degrees of freedom. However, we may easily adapt the proofs found in these references to show the following properties:

$$\nabla_h^P \cdot (\mathbf{V}_h^Q \times B)_p = 0 \ \ \forall P_p, \quad \nabla_h^{\Pi} \cdot (\mathbf{V}_h^Q \times B)_d = 0 \ \ \forall \Pi_d, \tag{30}$$

$$\langle \nabla_h^{P\Pi} \times \boldsymbol{E}, B\rangle_{P\Pi} = \langle \boldsymbol{E}, \mathbf{V}_h^Q \times B\rangle_Q + \langle \boldsymbol{E}\cdot\mathbf{t}, B\rangle_{\partial\Omega,h}. \tag{31}$$

5.3. Application to Maxwell's equations

The magnetic field unknowns B_p, B_d, B_s are located, respectively, on primal, dual cells and boundary primal sides while the electric field unknowns $\boldsymbol{E}_s, \boldsymbol{E}_d$ are located, respectively, on diamond cells and boundary dual cells. We use a leap-frog scheme for the time-discretization and the discrete operators defined in Section 5.2 for the space-discretization. This results in

$$B_p^{n+1} = B_p^n - \Delta t(\nabla_h^P \times \boldsymbol{E}^{n+1/2})_p, \tag{32}$$

$$B_d^{n+1} = B_d^n - \Delta t(\nabla_h^{\Pi} \times \boldsymbol{E}^{n+1/2})_d, \tag{33}$$

$$\varepsilon \boldsymbol{E}_s^{n+1/2} = \varepsilon \boldsymbol{E}_s^{n-1/2} + \Delta t \frac{1}{\mu}(\mathbf{V}_h^Q \times B^n)_s - \Delta t \boldsymbol{j}_s^n, \tag{34}$$

where $\boldsymbol{j}_s^n$ is a suitable approximation of $\boldsymbol{j}$. Moreover, the computed electric field $\boldsymbol{E}^{n+1/2}$ should ideally verify

$$\varepsilon(\nabla_h^{\Pi} \cdot \boldsymbol{E}^{n+1/2})_p = \rho_p^{n+1/2}, \tag{35}$$

$$\varepsilon(\nabla_h^{\Pi} \cdot \boldsymbol{E}^{n+1/2})_d = \rho_d^{n+1/2}, \tag{36}$$

where $(\rho_p^{n+1/2}, \rho_d^{n+1/2})$ is a suitable approximation of ρ. Thanks to the definitions of the discrete differential operators given in Section 5.2, it is quite easy to see that when $\varepsilon_p = \varepsilon_d = \varepsilon$ and $\mu_p = \mu_d = \mu$, then Eq. (32) is the same as the first line in (13), Eq. (33) is the same as the second line in (13) thanks to (4) and to the definition of $\bar{\varepsilon}_s$, and Eq. (34) is the same as the sixth and seventh equalities in (13), thanks to (4) and the definitions of c_s and s_s.

5.4. Properties of the discretized system

Proposition 1. *In the case of mutually orthogonal primal and dual meshes, the system (32)–(34) splits into two independent subsystems corresponding to two covolume schemes. Specializing to a rectangular Cartesian mesh, we obtain two Yee schemes on primal and dual meshes.*

Proposition 2. *If the initial conditions verify the discrete Gauss law given by (35) and (36) and if the discrete charge and current densities verify the following discrete charge conservation equation*

$$\rho_p^{n+1/2} = \rho_p^{n-1/2} - \Delta t(\nabla_h^{P\Pi} \cdot \boldsymbol{j}^n)_p, \tag{37}$$

$$\rho_d^{n+1/2} = \rho_d^{n-1/2} - \Delta t(\nabla_h^{P\Pi} \cdot \boldsymbol{j}^n)_d \tag{38}$$

for each $n \in \mathbb{N}$, then the scheme preserves the discrete Gauss law for each $n \in \mathbb{N}$.

Proof. We have just to apply the discrete primal (resp. dual) divergence to (34) and use the property (30). □

Proposition 3. *Suppose that: $\rho = 0$, $\boldsymbol{j} = 0$ and $\boldsymbol{E}\cdot\boldsymbol{t} = 0$ on $\partial\Omega$ (similar computations may be performed for other boundary conditions provided they are properly discretized). The following discrete electromagnetic energies are nonincreasing:*

$$\mathbb{E}_1^n = \frac{1}{2}\left(\varepsilon|\boldsymbol{E}^{n+1/2}|_Q^2 + \frac{1}{\mu}\langle B^n, B^{n+1}\rangle_{P\Pi}\right),$$

$$\mathbb{E}_2^n = \frac{1}{2}\left(\varepsilon\langle \boldsymbol{E}^{n+1/2}, \boldsymbol{E}^{n-1/2}\rangle_Q + \frac{1}{\mu}|B^n|_{P\Pi}^2\right).$$

Proof. From (34) we have

$$\varepsilon\left\langle \frac{\boldsymbol{E}^{n+1/2} - \boldsymbol{E}^{n-1/2}}{\Delta t}, \boldsymbol{E}^{n+1/2} + \boldsymbol{E}^{n-1/2}\right\rangle_Q = \frac{1}{\mu}\langle \nabla_h^Q \times B^n, \boldsymbol{E}^{n+1/2} + \boldsymbol{E}^{n-1/2}\rangle_Q,$$

so that according to the discrete Green formula (31):

$$\varepsilon(|\boldsymbol{E}^{n+1/2}|_Q^2 - |\boldsymbol{E}^{n-1/2}|_Q^2) = \Delta t \frac{1}{\mu}[\langle B^n, \nabla_h^{PII} \times \boldsymbol{E}^{n+1/2}\rangle_{PII} + \langle B^n, \nabla_h^{PII} \times \boldsymbol{E}^{n-1/2}\rangle_{PII} - \langle B^n, (\boldsymbol{E}^{n+1/2} + \boldsymbol{E}^{n-1/2}) \cdot \boldsymbol{t}\rangle_{\partial\Omega,h}].$$

The first line in the right-hand side of the previous expression may be transformed thanks to (32), (33), and since $\boldsymbol{E}^{n+1/2} \cdot \boldsymbol{t}$ vanishes on the boundary, the result is proved for $\mathbb{E}_1$. A similar proof may be performed for $\mathbb{E}_2$ starting from (32), (33) and using (31) the other way around. Since the discrete energies $\mathbb{E}_1^n$ and $\mathbb{E}_2^n$ are nonincreasing, proving that at least one of them is a positive definite quadratic form of the variables $\boldsymbol{E}^{n+1/2}$ and B^n is sufficient to prove the stability of the scheme. Indeed, this proves that there exists a positive constant C_h such that for all $n \in \mathbb{N}$

$$|\boldsymbol{E}^{n+1/2}|_D^2 + |B^n|_{PII}^2 \leqslant C_h|\mathbb{E}^n| \leqslant C_h|\mathbb{E}^0|. \tag{39}$$

This energy approach has previously been used, for example, in [31]. The stability of the scheme is proved in the Appendix using $\mathbb{E}_2$ and leads to the CFL condition (15). Since the computations with $\mathbb{E}_1$ are even more tedious, we skip the details and only give the final result. □

Proposition 4. *Under the CFL condition below, the scheme is stable*

$$c\Delta t \leqslant \min\left[\begin{array}{l} \min\limits_{\mathrm{p}} \max\left(\min\limits_{S_\mathrm{s}\in\partial P_\mathrm{p}\setminus\partial\Omega} \sqrt{\frac{2|\Sigma_\mathrm{s}|\|P_\mathrm{p}\|\cos\theta_\mathrm{s}}{n_\mathrm{p}|S_\mathrm{s}|(1+|\sin\theta_\mathrm{s}|)}}, \min\limits_{S_\mathrm{s}\in\partial P_\mathrm{p}\setminus\partial\Omega} \sqrt{\frac{2|\Sigma_\mathrm{s}|\|P_\mathrm{p}\|\cos\theta_\mathrm{s}}{(1+|\sin\theta_\mathrm{s}|)|\partial P_\mathrm{p}|}}\right) \\ \min\limits_{\mathrm{d}} \max\left(\min\limits_{\Sigma_\mathrm{s}\in\partial\Pi_\mathrm{d}} \sqrt{\frac{2|S_\mathrm{s}|\|\Pi_\mathrm{d}\|\cos\theta_\mathrm{s}}{n_\mathrm{d}|\Sigma_\mathrm{s}|(1+|\sin\theta_\mathrm{s}|)}}, \min\limits_{\Sigma_\mathrm{s}\in\Pi_\mathrm{d}} \sqrt{\frac{2|S_\mathrm{s}|\|\Pi_\mathrm{d}\|\cos\theta_\mathrm{s}}{(1+|\sin\theta_\mathrm{s}|)|\partial\Pi_\mathrm{d}|}}\right) \end{array}\right], \tag{40}$$

where n_p (resp., n_d) is the number of inner sides of the primal cell P_p (resp., of the dual cell Π_d), $|\partial P_\mathrm{p}|$ (resp., $|\partial\Pi_\mathrm{d}|$) is the sum of the lengths of the inner sides of P_p (resp., Π_d), and θ_s is the angle between $\mathbf{t}_\mathrm{s}$ and $\boldsymbol{v}_\mathrm{s}$ defined by $\boldsymbol{v}_\mathrm{s} := \frac{|\Sigma_{\mathrm{sp}}|\boldsymbol{v}_{\mathrm{sp}}+|\Sigma_{\mathrm{sq}}|\boldsymbol{v}_{\mathrm{sq}}}{\|\xi_\mathrm{p}\xi_\mathrm{q}\|}$ (see Fig. 3 for the notations).

6. Comparison with other methods

6.1. About the stability condition

The condition (40) is set on primal and dual cells, while condition (15) was set on diamond-cells. It is easy to verify that, in the case of a square mesh with edge length h, conditions (40) and (16) degenerate into that of Yee's scheme $c\Delta t \leqslant \frac{h\sqrt{2}}{2}$. In the case of a regular triangular mesh (equilateral triangles with edge length h), both conditions yield $c\Delta t \leqslant \frac{h\sqrt{6}}{6}$. In both cases, the condition is thus less restrictive, by a factor $\sqrt{2}$, than that given by the *cell-centered* first-order upwind finite volume scheme, see [64, Theorem 2.1]. On the other hand, the CFL condition for the *vertex-centered* first-order upwind finite volume scheme on a regular (primal) triangular mesh is $c\Delta t \leqslant \frac{h}{2}$, which is slightly better than that of the present scheme.

6.2. About the complexity of the algorithm

Let $N_\mathrm{p}, N_\mathrm{d}, N_\mathrm{s}$ be the number of primal cells, dual cells and primal sides. The total number of degrees of freedom (dof) in the present scheme is $N_\mathrm{p} + N_\mathrm{d} + 2N_\mathrm{s}$, while it would be $N_\mathrm{p} + N_\mathrm{s}$ for a Yee-type (covolume) scheme, $3N_\mathrm{p}$ for the cell-centered (upwind) finite volume scheme, and $3N_\mathrm{d}$ for the vertex-centered (upwind) finite volume scheme. Note that N_s equals $N_\mathrm{p} + N_\mathrm{d} - 1 + N_h$, where N_h is the number of holes in the domain Ω, thanks to Euler's formula. As far as triangular meshes are concerned, there holds $N_\mathrm{p} = \mathrm{O}(2N_\mathrm{d})$, while for quadrangular structured meshes, $N_\mathrm{p} = \mathrm{O}(N_\mathrm{d})$. Thus on triangular (resp. on quadrangular structured) meshes, the present scheme involves $\mathrm{O}(9N_\mathrm{p}/2)$ (resp. $\mathrm{O}(6N_\mathrm{p})$) dof, while the cell-centered finite volume scheme involves $3N_\mathrm{p}$ (resp. $3N_\mathrm{p}$) dof, the vertex-centered finite volume scheme involves $\mathrm{O}(3N_\mathrm{p}/2)$ (resp. $3N_\mathrm{p}$) dof, and the covolume scheme involves $\mathrm{O}(5N_\mathrm{p}/2)$ (resp. $\mathrm{O}(3N_\mathrm{p})$) dof.

Moreover, computing $B^{n+1}, \boldsymbol{E}^{n+1/2}$ from the known values of $B^n, \boldsymbol{E}^{n-1/2}$ does not require a very complex algorithm, since the operators $\nabla_h^P\times, \nabla_h^{\Pi}\times$ and $\mathbf{V}_h^Q\times$ used in (32)–(34) have fairly simple stencils, which are usually given by (or may easily be constructed from) the output of standard mesh generators.

Of course, the comparison between various schemes should not be limited to issues concerning their complexity and number of unknowns on a given mesh, but should include a discussion on the overall computational effort required to obtain a prescribed accuracy on a prescribed family of meshes. As far as the comparison with a standard FDTD scheme (possibly with boundary fixes to account for non orthogonal boundaries) is concerned, the following point has to be mentioned: Since on Cartesian rectangular meshes the scheme we present here decouples into two independent FDTD schemes (the first being cell-centered and the second vertex-centered), we may not expect any accuracy improvement over a standard FDTD scheme on such a mesh, while doubling the number of unknowns will double the price of the algorithm. The present method will thus be useful in applications where the use of Cartesian rectangular meshes is not possible (because the mesh is *given*, for example through a coupling with another model) or expensive (because highly refined, possibly non-conforming, cells are needed in the vicinity of a singularity or of a stiff source term).

These are actually the cases treated in the next section: distorted and non-conforming *given* families of meshes (Section 7.1) and highly refined non-conforming meshes in the vicinity of a stiff source term (Section 7.2).

7. Numerical experiments

Define the discrete L_2-norm by

$$\|u\|_2 = \left(\sum_{\mathrm{p}} \|P_{\mathrm{p}}\| u_{\mathrm{p}}^2 + \sum_{\mathrm{d}} \|\Pi_{\mathrm{d}}\| u_{\mathrm{d}}^2 \right)^{\frac{1}{2}}$$

and the discrete L_∞-norm by

$$\|u\|_\infty = \max_{\mathrm{p,d}} (|u_{\mathrm{p}}|, |u_{\mathrm{d}}|).$$

Let N be the number of cells and define by h the following characteristic length associated with the mesh

$$h = \left(\frac{\|\Omega\|}{N} \right)^{\frac{1}{2}}.$$

The relative errors between the exact solution u_e^n and the approximated one u_h^n at time $n\Delta t$ are defined by

$$e_{h,2}^n = \frac{\|u_h^n - u_e^n\|_2}{\|u_e^n\|_2}, \quad e_{h,\infty}^n = \frac{\|u_h^n - u_e^n\|_\infty}{\|u_e^n\|_\infty}.$$

The relative errors between the times T_1 and T_2 are defined by

$$e_{h,2} = \left(\frac{\sum_{T_1 \leqslant n\Delta t \leqslant T_2} \|u_h^n - u_e^n\|_2^2}{\sum_{T_1 \leqslant n\Delta t \leqslant T_2} \|u_e^n\|_2^2} \right)^{\frac{1}{2}}, \quad e_{h,\infty} = \frac{\sum_{T_1 \leqslant n\Delta t \leqslant T_2} \|u_h^n - u_e^n\|_\infty}{\sum_{T_1 \leqslant n\Delta t \leqslant T_2} \|u_e^n\|_\infty}. \tag{41}$$

The order of the method is given by

$$\text{order} = \frac{\log(e_{2h}) - \log(e_h)}{\log 2}.$$

The three benchmarks we present aim at illustrating the good behavior of the method when Maxwell's equations (possibly in inhomogeneous media or with stiff solutions) have to be approximated on distorted or non-conforming meshes. Comparisons with the Yee scheme have been carried out (whenever rectangle meshes are used, since for such meshes our method coincides with the Yee scheme).

In what follows, all physical quantities are expressed in the MKSA units. The values $\varepsilon_0 = 8.8542 \times 10^{-12}$ and $\mu_0 = 1.2566 \times 10^{-6}$ are the permittivity and the permeability of the free space and $c = (\varepsilon_0 \mu_0)^{-\frac{1}{2}}$ is the velocity of light.

7.1. Eigenmodes of an inhomogeneous unit square

Suppose that $\Omega = [0,1]^2$ and consider the model problem (5). Given $k = l = 2$, let us define the pulsation

$$\omega = \pi \left(\frac{k^2 + l^2}{\varepsilon \mu} \right)^{\frac{1}{2}}$$

and the permittivity and permeability

$$\begin{cases} \varepsilon = \varepsilon_0, \quad \mu = \mu_0 \quad \text{if } x \leqslant 0.5, \\ \varepsilon = 2\varepsilon_0, \quad \mu = \frac{1}{2}\mu_0 \quad \text{if } x > 0.5. \end{cases}$$

In order to get a simple analytic solution we have chosen ε and μ such that the speed of light is the same in both media. Other arbitrary ε and μ could be chosen as well. The initial fields are

$$\begin{cases} B^0 = \mu H^0 = \cos(\pi k x)\cos(\pi l y) \quad \text{if } x \leqslant 0.5, \\ B^0 = \mu H^0 = \frac{1}{2}\cos(\pi k x)\cos(\pi l y) \quad \text{if } x > 0.5, \\ \boldsymbol{D}^0 = \varepsilon \boldsymbol{E}^0 = \boldsymbol{0}, \\ \rho = 0, \quad \boldsymbol{j} = \boldsymbol{0}, \\ \alpha = 1, \quad \beta = 0, \quad g = 0 \quad \text{(perfect conductor boundary condition)} \end{cases}$$

and the solution of (5) is

$$\begin{cases} B = \mu H = \cos(\pi k x)\cos(\pi l y)\cos(\omega t) \quad \text{if } x \leqslant 0.5, \\ B = \mu H = \frac{1}{2}\cos(\pi k x)\cos(\pi l y)\cos(\omega t) \quad \text{if } x > 0.5, \\ D_x = \varepsilon E_x = -\frac{l\pi}{\mu_0 \omega}\cos(\pi k x)\sin(\pi l y)\sin(\omega t), \\ D_y = \varepsilon E_y = \quad \frac{k\pi}{\mu_0 \omega}\sin(\pi k x)\cos(\pi l y)\sin(\omega t). \end{cases}$$

We will use eight groups of meshes of the unit square that respect the boundary ($x = 0.5$) between both media (see Fig. 4: for all these meshes the primal points are the centers of gravity of the convex primal cells and the midpoints of the interior diagonal of the non-convex quadrilaterals).

1. Square meshes.
2. Non-conforming rectangle meshes.
3. Distorted convex quadrilateral meshes (the refinement is performed by dividing each quadrilateral into four quadrilaterals).
4. Distorted triangular meshes constructed by dividing each quadrilateral of the previous meshes into four triangles.
5. Right triangle meshes.
6. Randomly distorted quadrilateral meshes (the interior vertices are randomly moved). Note that such meshes can include non-convex quadrilaterals.
7. Randomly distorted triangle meshes (the interior vertices are randomly moved).
8. Strongly non-convex quadrilateral meshes, constructed from the previous square meshes in such a way that the center (x, y) of each motif of four squares is replaced by $(x + \Delta x(1 + \cos\theta), y + \Delta y(1 + \sin\theta)), \Delta x = \Delta y$ being the length of the square sides and $\theta = 0.25\pi$.

We have chosen

$$T = 20 \times \frac{2\pi}{\omega} \simeq 4.71734 \times 10^{-8}.$$

The relative errors for the magnetic field H between the times $38\frac{\pi}{\omega}$ and $40\frac{\pi}{\omega}$ are given in Tables 1 and 2 and deserve some discussion (similar errors have been obtained for the electric field $\boldsymbol{D}$). The numerical analysis of this scheme has been conducted and will be reported elsewhere; one may also refer to Ref. [7] since it considers the special case of orthogonal primal–dual meshes. The theoretical results we obtain help us understand (at least partially) the numerical results presented in Tables 1 and 2. Indeed, we may prove that, under the uniformity with respect to h of the constant C_h in (39), the L^2 norm of the error in the computed solution at the final time of the simulation may be bounded by a term which typically behaves like $C(\theta)h^{\alpha}$, where h is the mesh step size, θ is the largest (in absolute value) in the angles θ_{sp} and θ_{sq} (see Fig. 3), when s runs over all possible edges of the mesh. When θ tends to $\pi/2$, i.e. when the mesh is very distorted, $C(\theta)$ tends to $+\infty$, otherwise it is bounded. We are able to prove that the order of convergence α is at least 1 for general meshes and at least 1.5 if the meshes are more regular or tend to be more regular when refined. Here, more regular means that the diamond-cells are almost all parallelograms (note that boundary diamond-cells cannot be parallelograms, which explains the order 1.5 instead of 2) and that the vertices x_{d} of the primal mesh are the centroids of their associated dual cells Π_{d}. These theoretical results are probably suboptimal in view of the numerical results which indicate second-order convergence; however they help us understand the somehow "erratic" convergence on the random quadrangular and triangular meshes, since these families experience large variations in the values of their angles θ, which implies large variations in the function $C(\theta)$.

Fig. 5 displays the magnetic field $H = H(T)$ for the eight meshes displayed on Fig. 4 (with 80^2 cells). The slight oscillations that may be observed on some meshes are an effect of the visualization due to underlying distorted meshes (the same phenomenon is observed with the analytic solution).

7.2. Radiation from a dipole

Suppose that $\Omega = [-1, 1]^2$. Let $r = (x^2 + y^2)^{\frac{1}{2}}, r_0 = 0.25$ and $F(r)$ the function such that $F(r) = 1$ if $r \leqslant r_0$ and $F(r) = 0$ if $r > r_0$. Given

$$\omega = \pi\left(\frac{k^2 + l^2}{\varepsilon_0 \mu_0}\right)^{\frac{1}{2}}$$

and

$$\begin{cases} B^0 = \mu_0 H^0 = \cos(\pi k x)\cos(\pi l y) + \frac{4}{\varepsilon_0 \mu_0 \omega^2}\frac{r_0^2(r_0^4 - r^4 - r_0^2 r^2)}{(r_0^2 - r^2)^4}\exp\left(-\frac{r^2}{r_0^2 - r^2}\right)F(r), \\ \boldsymbol{D}^0 = \varepsilon_0 \boldsymbol{E}^0 = \boldsymbol{0}, \\ j_x = \frac{2}{\mu_0}\frac{r_0^2}{(r_0^2 - r^2)^2}\left(1 + \frac{4}{\varepsilon_0 \mu_0 \omega^2}\frac{2r^6 + 4r_0^2 r^4 - 7r_0^4 r^2 + 2r_0^6}{(r_0^2 - r^2)^4}\right)\exp\left(-\frac{r^2}{r_0^2 - r^2}\right)F(r) y \cos(\omega t), \\ j_y = -\frac{2}{\mu_0}\frac{r_0^2}{(r_0^2 - r^2)^2}\left(1 + \frac{4}{\varepsilon_0 \mu_0 \omega^2}\frac{2r^6 + 4r_0^2 r^4 - 7r_0^4 r^2 + 2r_0^6}{(r_0^2 - r^2)^4}\right)\exp\left(-\frac{r^2}{r_0^2 - r^2}\right)F(r) x \cos(\omega t), \\ \alpha = 1, \quad \beta = 0, \quad g = 0 \quad (\text{perfect conductor boundary condition}), \end{cases}$$

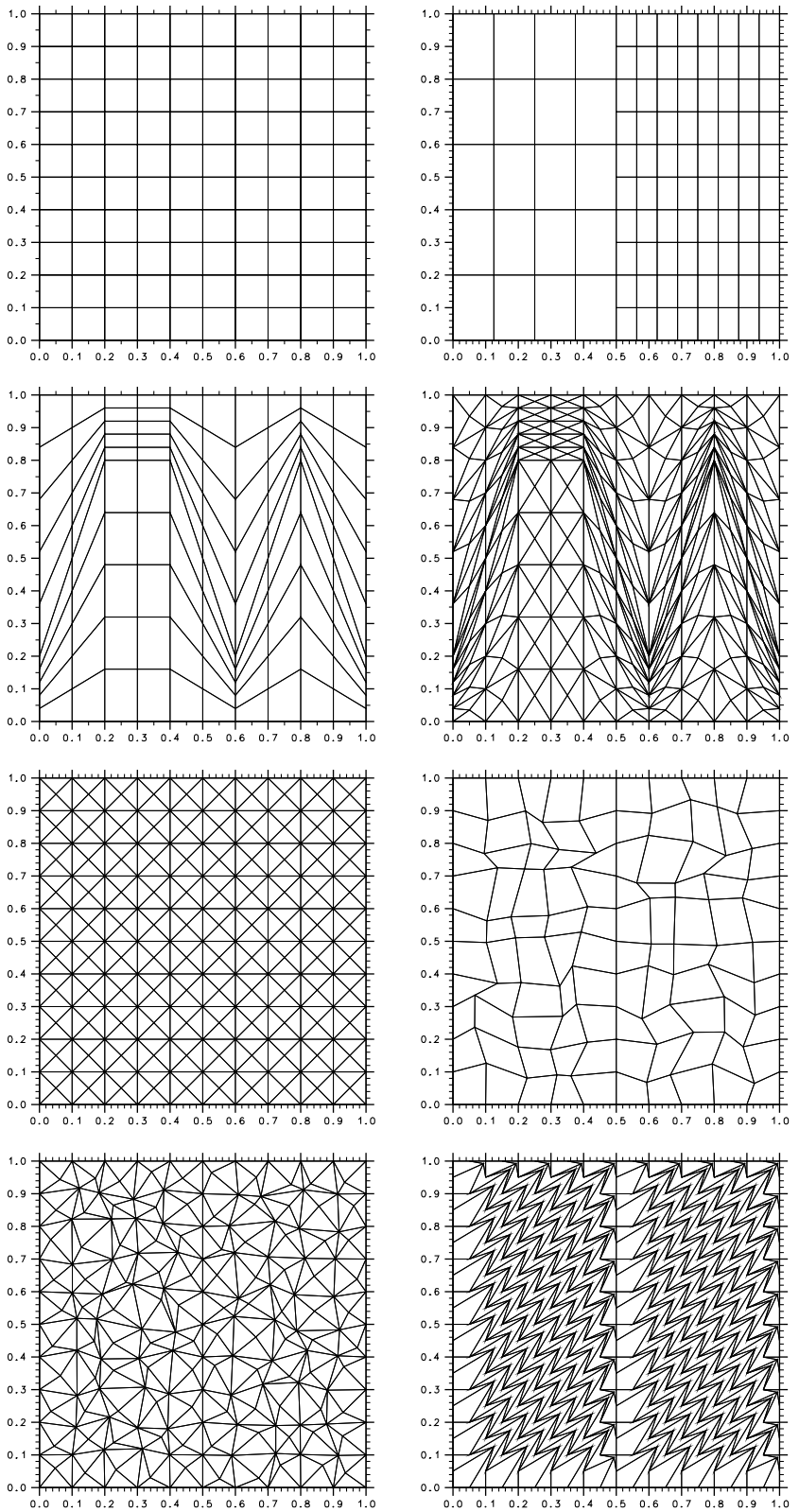

Fig. 4. Coarse meshes of the unit square.

Table 1
Relative errors for the magnetic field H

h^{-1}	Square meshes	Order	Non-conforming quadrilateral meshes	Order	Distorted quadrilateral meshes	Order	Distorted triangle meshes	Order
$e_{h,2}$								
10	9.66×10^{-1}		1.52×10^{0}		1.43×10^{0}			
20	2.58×10^{-1}	1.90	6.00×10^{-1}	1.34	1.23×10^{0}	0.22	1.51×10^{0}	
40	6.36×10^{-2}	2.02	1.51×10^{-1}	1.98	3.39×10^{-1}	1.86	5.16×10^{-1}	1.55
80	1.47×10^{-2}	2.11	3.65×10^{-2}	2.05	8.29×10^{-2}	2.03	1.28×10^{-1}	2.01
160	2.44×10^{-3}	2.57	7.90×10^{-3}	2.20	1.94×10^{-2}	2.09	3.06×10^{-2}	2.06
320	5.95×10^{-4}	2.05	7.66×10^{-4}	3.36	3.66×10^{-3}	2.40	6.45×10^{-3}	2.25
$e_{h,\infty}$								
10	8.56×10^{-1}		1.66×10^{0}		2.07×10^{0}			
20	2.28×10^{-1}	1.90	5.70×10^{-1}	1.54	1.35×10^{0}	0.22	1.69×10^{0}	
40	5.66×10^{-2}	2.01	1.43×10^{-1}	1.99	3.63×10^{-1}	1.86	5.14×10^{-1}	1.71
80	1.31×10^{-2}	2.11	3.43×10^{-2}	2.05	8.93×10^{-2}	2.03	1.27×10^{-1}	2.01
160	2.23×10^{-3}	2.55	7.48×10^{-3}	2.20	2.12×10^{-2}	2.09	3.07×10^{-2}	2.04
320	5.40×10^{-4}	2.04	8.21×10^{-4}	3.19	4.28×10^{-3}	2.40	6.69×10^{-3}	2.20

Table 2
Relative errors for the magnetic field H

h^{-1}	Right triangle meshes	Order	Randomly quadrilateral meshes	Order	Randomly triangle meshes	Order	Non-convex quadrilateral meshes	Order
$e_{h,2}$								
10			1.17×10^{0}					
20	7.63×10^{-1}		2.82×10^{-1}	2.06	1.06×10^{0}		1.33×10^{0}	
40	2.05×10^{-1}	1.89	8.13×10^{-2}	1.79	2.01×10^{-1}	2.39	1.01×10^{0}	0.39
80	5.05×10^{-2}	2.02	1.06×10^{-2}	2.94	9.71×10^{-2}	1.05	2.70×10^{-1}	1.90
160	1.16×10^{-2}	2.12	9.92×10^{-3}	0.09	2.25×10^{-2}	2.11	6.63×10^{-2}	2.03
320	1.98×10^{-3}	2.54	1.15×10^{-3}	3.11	6.24×10^{-3}	1.85	1.53×10^{-2}	2.11
$e_{h,\infty}$								
10			1.14×10^{0}					
20	9.12×10^{-1}		2.76×10^{-1}	2.05	1.29×10^{0}		1.63×10^{0}	
40	2.42×10^{-1}	1.91	7.90×10^{-2}	1.84	2.50×10^{-1}	2.37	1.07×10^{0}	0.60
80	5.96×10^{-2}	2.02	1.22×10^{-2}	2.69	1.06×10^{-1}	1.23	2.82×10^{-1}	1.92
160	1.38×10^{-2}	2.10	9.83×10^{-3}	0.31	2.67×10^{-2}	1.98	6.95×10^{-2}	2.02
320	2.42×10^{-3}	2.52	1.97×10^{-3}	2.32	9.01×10^{-3}	1.57	1.64×10^{-2}	2.08

the solution of (5) is

$$\begin{cases} B = \mu_0 H = \left(\cos(\pi k x)\cos(\pi l y) + \frac{4}{\varepsilon_0 \mu_0 \omega^2} \frac{r_0^2(r_0^4 - r^4 - r_0^2 r^2)}{(r_0^2 - r^2)^4} \exp\left(-\frac{r^2}{r_0^2 - r^2}\right) F(r)\right) \cos(\omega t), \\ D_x = \varepsilon_0 E_x = \left(-\frac{l\pi}{\mu_0 \omega}\cos(\pi k x)\sin(\pi l y) - \frac{2}{\mu_0 \omega} \frac{r_0^2 y}{(r_0^2 - r^2)^2} \exp\left(-\frac{r^2}{r_0^2 - r^2}\right) F(r)\right) \sin(\omega t), \\ D_y = \varepsilon_0 E_y = \left(\frac{k\pi}{\mu_0 \omega}\sin(\pi k x)\cos(\pi l y) + \frac{2}{\mu_0 \omega} \frac{r_0 x}{(r_0^2 - r^2)^2} \exp\left(-\frac{r^2}{r_0^2 - r^2}\right) F(r)\right) \sin(\omega t). \end{cases}$$

Note that such functions have strong peaks near the center of Ω: Fig. 6 shows the value of the magnetic field along the axis $y = 0$.

We consider the subdomain $\Omega_0 = [-1/4, 1/4]$ and we uniformly mesh $\Omega \setminus \Omega_0$ with squares of size h, and Ω_0 with squares of size $h_0 = h/2^p$. Fig. 7 displays such a mesh with $p = 2$.

First, we set $h = 1/32$ and let h_0 tend to zero as long as the error significantly decreases. As a second test, we fix $h_0 = 1/128$ and coarsen the mesh covering $\Omega \setminus \Omega_0$ until the error starts to increase significantly. We let the simulations run over 10 periods of the wave and display in Fig. 8 the relative L^2 norms of the errors $e_{h,2}(B)$ and $e_{h,2}(\boldsymbol{E})$, defined by (41), averaged over the last period, with $T_1 = 9T$ and $T_2 = 10T$.

We plot the curves representing the first test with plain lines and those representing the second test with dashed lines.

According to these figures, we can deduce that the best refinement ratio for this example is $h/h_0 = 4$. So we choose to study the L^2 convergence on a family of meshes having that refinement ratio: we set $h/h_0 = 4$ and let h and h_0 tend to zero. Fig. 9 shows that the scheme has a second-order convergence for such kind of meshes.

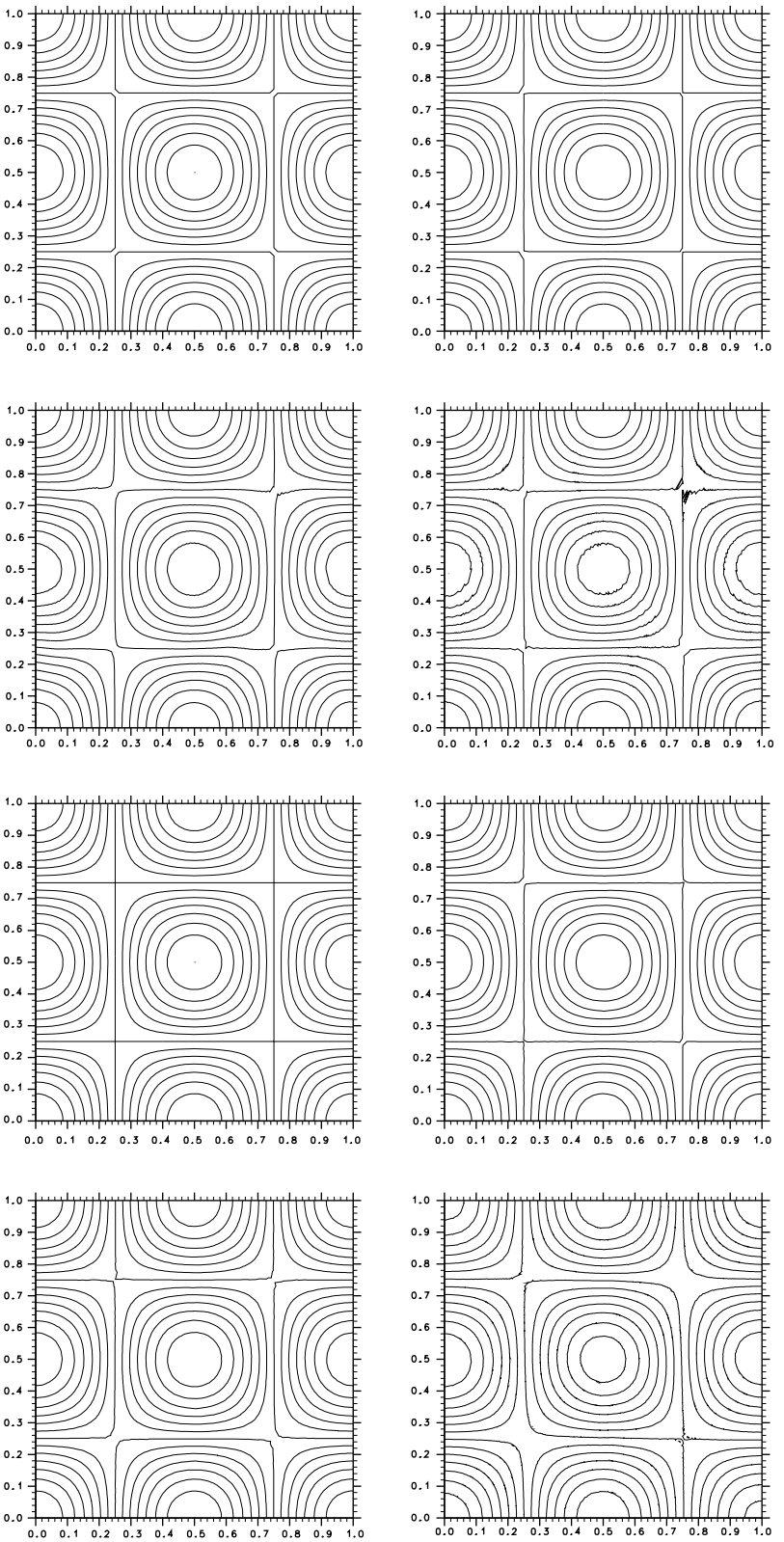

Fig. 5. Isovalues of $H(t = 40\frac{\pi}{\omega})$ on the meshes displayed on Fig. 4 with 80^2 cells.

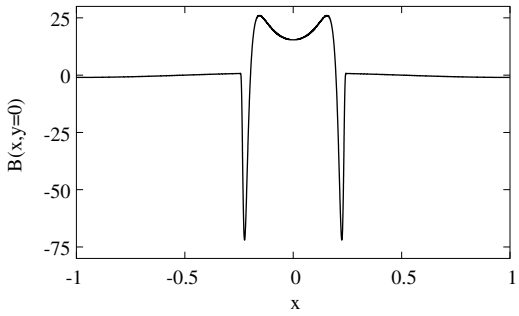

Fig. 6. Values of B along $y = 0$.

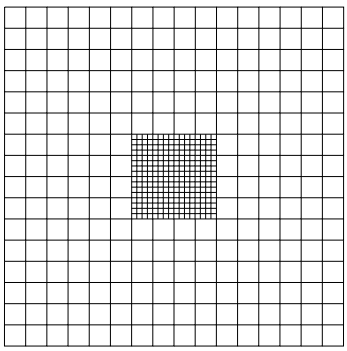

Fig. 7. A mesh with $h = 1/8$ and $h_0 = 1/32$.

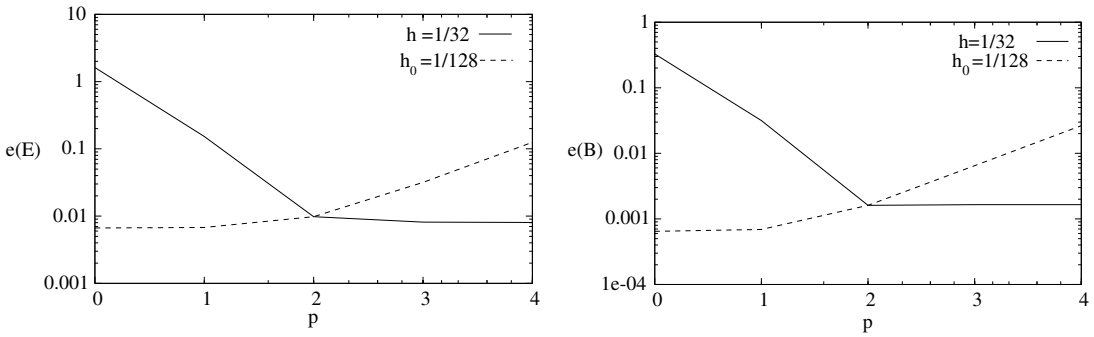

Fig. 8. L^2 norm of the error on $\boldsymbol{E}$ (left) and B (right) according to p in logarithmic scale.

7.3. Ingoing wave

Suppose that $\Omega = [-1, 1]^2$. Given

$$\omega = \pi\left(\frac{k^2 + l^2}{\varepsilon_0\mu_0}\right)^{\frac{1}{2}}$$

and

$$\begin{cases} B^0 = 0, \quad \boldsymbol{D}^0 = \varepsilon_0\boldsymbol{E}^0 = \boldsymbol{0}, \\ \rho = 0, \quad \boldsymbol{j} = \boldsymbol{0}, \\ \alpha = 1, \quad \beta = \left(\frac{\mu_0}{\varepsilon_0}\right)^{\frac{1}{2}}, \quad g = -2\sin\left(\omega\left(\frac{x}{c} - t\right)\right) \quad \text{on the left side}, \\ \alpha = 1, \quad \beta = \left(\frac{\mu_0}{\varepsilon_0}\right)^{\frac{1}{2}}, \quad g = 0 \quad \text{on the right side}, \\ \alpha = 1, \quad \beta = 0 \quad , g = 0 \quad \text{on the other sides}, \end{cases}$$

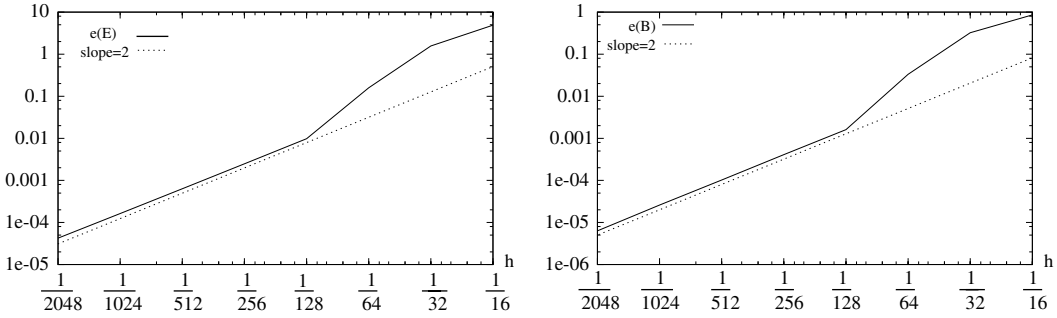

Fig. 9. Convergence on the discrete L^2 norm (left: $\boldsymbol{E}$, right: B).

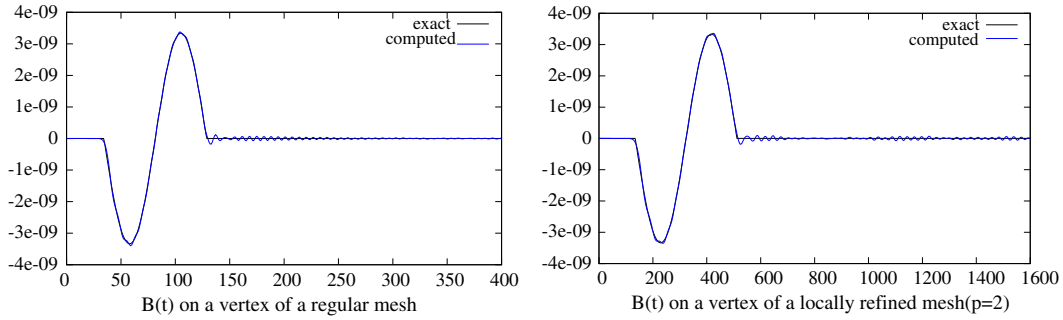

Fig. 10. Comparison of parasitic reflexions on a Cartesian mesh (left) and a locally refined mesh (right).

one can check that

$$\begin{cases} B = \mu_0 H = \frac{1}{c}\sin\left(\omega\left(\frac{x}{c} - t\right)\right), \\ D_x = \varepsilon_0 E_x = 0, \\ D_y = \varepsilon_0 E_y = \varepsilon_0 \sin\left(\omega\left(\frac{x}{c} - t\right)\right) \end{cases}$$

is the solution of (5).

We have chosen $k = l = 1$ and we let the wave enter during one period only. The intensity of the magnetic field on a vertex of the mesh is plotted in Fig. 10. The left part of this figure concerns the propagation of the wave on square mesh, while the right part concerns a non-conforming locally refined mesh like that displayed in Fig. 7. We repeated the test on different points and meshes, and we get similar results. This shows that local refinement does not amplify the amplitude of parasitic reflexions.

8. Concluding remarks

We have proposed a second-order accurate finite volume type method that allows nearly arbitrary meshes to be considered for solving Maxwell's equations in two space dimensions. Thanks to this property, non-conforming meshes, particularly, can be used without inconvenient.

Since both the normal and the tangential components of the electromagnetic field are taken into account, we think that such a method is well suited for dealing with anisotropic media. Moreover it could be a qualified candidate for approximating other wave equations like the acoustics equations or the linearized Saint–Venant equations with the Coriolis force term on arbitrary meshes.

Appendix A. The 3-D case

In this appendix we outline what could be a generalization of our method to the 3-D case. Finite volume methods of this type have been proposed and tested in [65–67].

Like the 2-D case let us consider both a primal mesh and a dual mesh that is made up from the primal mesh. Let denote by (see Fig. 11):

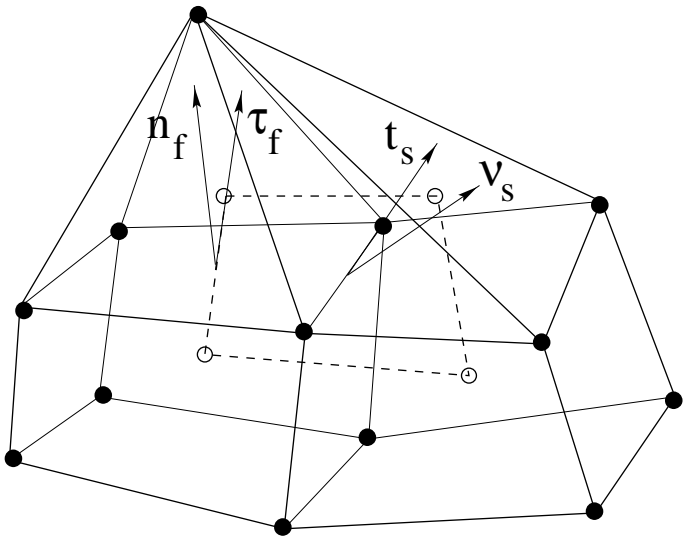

Fig. 11. A sample 3-D primal mesh made up of two pyramids and two hexahedra (solid lines) and a face of its dual mesh (dashed lines).

- $F_f(\Phi_s)$ the primal (dual) faces,
- $\Sigma_f(S_s)$ the dual (primal) sides associated with the primal (dual) faces $F_f(\Phi_s)$,
- $\boldsymbol{n}_f(\boldsymbol{\nu}_s)$ the unit outward normal vector through the face $F_f(\Phi_s)$,
- $\boldsymbol{t}_s(\boldsymbol{\tau}_f)$ the unit tangent vector along the side $S_s(\Sigma_f)$.

Taking the flux of Maxwell's equations (Faraday and Ampere–Maxwell laws) over each primal F_f *and* dual face Φ_s and using the Stokes theorem results in

$$\begin{cases} \frac{\partial}{\partial t}\left(\int\int_{F_f} \boldsymbol{B}_f \cdot n_f\right) + \sum\limits_{S_s \in \partial F_f} \int_{S_s} \boldsymbol{E}_s \cdot t_s = 0, \\ \frac{\partial}{\partial t}\left(\int\int_{\Phi_s} \boldsymbol{B}_s \cdot \nu_s\right) + \sum\limits_{\Sigma_f \in \partial \Phi_s} \int_{\Sigma_f} \boldsymbol{E}_f \cdot \tau_f = 0, \\ \frac{\partial}{\partial t}\left(\int\int_{F_f} \boldsymbol{E}_f \cdot n_f\right) - \sum\limits_{S_s \in \partial F_f} \int_{S_s} \boldsymbol{B}_s \cdot t_s = -\int\int_{F_f} j \cdot n_f, \\ \frac{\partial}{\partial t}\left(\int\int_{\Phi_s} \boldsymbol{E}_s \cdot \nu_s\right) - \sum\limits_{\Sigma_f \in \partial \Phi_s} \int_{\Sigma_f} \boldsymbol{B}_f \cdot \tau_f = -\int\int_{\Phi_s} \boldsymbol{j} \cdot \nu_s. \end{cases}$$

The *main* unknowns of this system are $\boldsymbol{B}_f \cdot \boldsymbol{n}_f, \boldsymbol{B}_s \cdot \boldsymbol{\nu}_s, \boldsymbol{E}_f \cdot \boldsymbol{n}_f, \boldsymbol{E}_s \cdot \boldsymbol{\nu}_s$ while the *auxiliary* unknowns $\boldsymbol{E}_s \cdot \boldsymbol{t}_s, \boldsymbol{E}_f \cdot \boldsymbol{\tau}_f, \boldsymbol{B}_s \cdot \boldsymbol{t}_s, \boldsymbol{B}_f \cdot \boldsymbol{\tau}_f$, may be calculated from the main unknowns. For example the whole vector $\boldsymbol{B}_f$ ($\boldsymbol{E}_f$) can be calculated in the neighborhood of the face F_f from the main unknowns $\boldsymbol{B}_f \cdot \boldsymbol{n}_f$ ($\boldsymbol{E}_f \cdot \boldsymbol{n}_f$) and $\boldsymbol{B}_s \cdot \boldsymbol{\nu}_s$ ($\boldsymbol{E}_s \cdot \boldsymbol{\nu}_s$) for $S_s \in \partial F_f$, by using a least square method. Similarly the whole vector $\boldsymbol{B}_s$ ($\boldsymbol{E}_s$) can be calculated in the neighborhood of the face Φ_s from the main unknowns $\boldsymbol{B}_s \cdot \boldsymbol{\nu}_s$ ($\boldsymbol{E}_s \cdot \boldsymbol{\nu}_s$) and $\boldsymbol{B}_f \cdot \boldsymbol{n}_f$ ($\boldsymbol{E}_f \cdot \boldsymbol{n}_f$) for $\Sigma_f \in \partial \Phi_s$.

Note that such a method preserves the divergence. Furthermore it boils down in two independent methods when the primal and dual meshes are orthogonal ($\boldsymbol{n}_f = \boldsymbol{\tau}_f$ and $\boldsymbol{\nu}_s = \boldsymbol{t}_s$), the first of these being the method proposed in [3,6].

Appendix B. Stability condition

The proof of the stability condition (15) is now detailed. Consider a homogeneous medium and suppose that $\boldsymbol{j} = \boldsymbol{0}$. The total electromagnetic energy which appears in (14) may obviously be split into magnetic and electric contributions.

Splitting the sums over primal and dual cells into sums over half diamond-cells, provides the following expression of the discrete magnetic energy at time $(n+1)\Delta t$

$$\frac{1}{4}\mu\left(\sum_{P_p} \|P_p\|(H_p^{n+1})^2 + \sum_{\Pi_d} \|\Pi_d\|(H_d^{n+1})^2\right) = \frac{1}{4}\mu\sum_{Q_{sp}} \|Q_{sp}\|(H_p^{n+1})^2 + \frac{1}{4}\mu\sum_{Q_{sq}} \|Q_{sq}\|(H_q^{n+1})^2 + \frac{1}{8}\mu\sum_{Q_{sp}} \|Q_{sp}\|((H_d^{n+1})^2 + (H_e^{n+1})^2) + \frac{1}{8}\mu\sum_{Q_{sq}} \|Q_{sq}\|\left((H_d^{n+1})^2 + (H_e^{n+1})^2\right).$$

As far as the discrete electric energy is concerned, starting from (13) and setting $N_s^{n+\frac{1}{2}} = \boldsymbol{E}_s^{n+\frac{1}{2}} \cdot \boldsymbol{n}_s$ and $T_s^{n+\frac{1}{2}} = \boldsymbol{E}_s^{n+\frac{1}{2}} \cdot \boldsymbol{t}_s$, leads to

$$\begin{cases} \varepsilon\|Q_s\|N_s^{n+\frac{1}{2}} = \varepsilon\|Q_s\|N_s^{n-\frac{1}{2}} + \frac{1}{2}\Delta t c_s|\Sigma_s|(H_e^n - H_d^n), \\ \varepsilon\|Q_s\|T_s^{n+\frac{1}{2}} = \varepsilon\|Q_s\|T_s^{n-\frac{1}{2}} - \frac{1}{2}\Delta t|S_s|(H_q^n - H_p^n) + \frac{1}{2}\Delta t s_s|\Sigma_s|(H_e^n - H_d^n). \end{cases} \tag{42}$$

Consider now the equations in (42) written at time $n+\frac{3}{2}$ and multiply them, respectively, by

$$\frac{1}{2}N_s^{n+\frac{1}{2}} \quad \text{and} \quad \frac{1}{2}T_s^{n+\frac{1}{2}}.$$

We obtain

$$\begin{cases} \varepsilon\frac{1}{2}\|Q_s\|N_s^{n+\frac{3}{2}}N_s^{n+\frac{1}{2}} = \frac{1}{2}\varepsilon\|Q_s\|(N_s^{n+\frac{1}{2}})^2 + \frac{1}{4}\Delta t c_s|\Sigma_s|(H_e^{n+1} - H_d^{n+1})N_s^{n+\frac{1}{2}}, \\ \frac{1}{2}\varepsilon\|Q_s\|T_s^{n+\frac{3}{2}}T_s^{n+\frac{1}{2}} = \frac{1}{2}\varepsilon\|Q_s\|(T_s^{n+\frac{1}{2}})^2 - \frac{1}{4}\Delta t|S_s|(H_q^{n+1} - H_p^{n+1})T_s^{n+\frac{1}{2}} + \frac{1}{4}\Delta t s_s|\Sigma_s|(H_e^{n+1} - H_d^{n+1})T_s^{n+\frac{1}{2}}, \end{cases} \tag{43}$$

From (43) we deduce the following expression of the discrete electric energy at time $(n+1)\Delta t$

$$\begin{aligned} \frac{1}{2}\varepsilon\sum_{Q_s}\|Q_s\|\boldsymbol{E}_s^{n+\frac{3}{2}}\cdot\boldsymbol{E}_s^{n+\frac{1}{2}} &= \frac{1}{2}\varepsilon\sum_{Q_s}\|Q_s\|(N_s^{n+\frac{3}{2}}N_s^{n+\frac{1}{2}} + T_s^{n+\frac{3}{2}}T_s^{n+\frac{1}{2}}) = \frac{1}{2}\varepsilon\sum_{Q_{sp}}\|Q_{sp}\|\left((N_s^{n+\frac{1}{2}})^2 + (T_s^{n+\frac{1}{2}})^2\right) \\ &+ \frac{1}{2}\varepsilon\sum_{Q_{sq}}\|Q_{sq}\|\left((N_s^{n+\frac{1}{2}})^2 + (T_s^{n+\frac{1}{2}})^2\right) + \frac{1}{4}\Delta t\sum_{\Sigma_{sp}}c_{sp}|\Sigma_{sp}|(H_e^{n+1} - H_d^{n+1})N_s^{n+\frac{1}{2}} + \frac{1}{4}\Delta t\sum_{\Sigma_{sq}}c_{sq}|\Sigma_{sq}|(H_e^{n+1} - H_d^{n+1})N_s^{n+\frac{1}{2}} \\ &- \frac{1}{4}\Delta t\sum_{S_s}|S_s|(H_q^{n+1} - H_p^{n+1})T_s^{n+\frac{1}{2}} + \frac{1}{4}\Delta t\sum_{\Sigma_{sp}}s_{sp}|\Sigma_{sp}|(H_e^{n+1} - H_d^{n+1})T_s^{n+\frac{1}{2}} + \frac{1}{4}\Delta t\sum_{\Sigma_{sq}}s_{sq}|\Sigma_{sq}|(H_e^{n+1} - H_d^{n+1})T_s^{n+\frac{1}{2}}. \end{aligned}$$

Thus, we obtain the following expression of the total electromagnetic energy at time $(n+1)\Delta t$

$$\begin{aligned} \int\int_\Omega U^{n+1} &= \frac{1}{4}\mu\sum_{Q_{sp}}\|Q_{sp}\|(H_p^{n+1})^2 + \frac{1}{4}\mu\sum_{Q_{sq}}\|Q_{sq}\|(H_q^{n+1})^2 + \frac{1}{8}\mu\sum_{Q_{sp}}\|Q_{sp}\|((H_d^{n+1})^2 + (H_e^{n+1})^2) \\ &+ \frac{1}{8}\mu\sum_{Q_{sq}}\|Q_{sq}\|\left((H_d^{n+1})^2 + (H_e^{n+1})^2\right) + \frac{1}{2}\varepsilon\sum_{Q_{sp}}\|Q_{sp}\|\left((N_s^{n+\frac{1}{2}})^2 + (T_s^{n+\frac{1}{2}})^2\right) + \frac{1}{2}\varepsilon\sum_{Q_{sq}}\|Q_{sq}\|\left((N_s^{n+\frac{1}{2}})^2 + (T_s^{n+\frac{1}{2}})^2\right) \\ &+ \frac{1}{4}\Delta t\sum_{\Sigma_{sp}}c_{sp}|\Sigma_{sp}|(H_e^{n+1} - H_d^{n+1})N_s^{n+\frac{1}{2}} + \frac{1}{4}\Delta t\sum_{\Sigma_{sq}}c_{sq}|\Sigma_{sq}|(H_e^{n+1} - H_d^{n+1})N_s^{n+\frac{1}{2}} - \frac{1}{4}\Delta t\sum_{S_s}|S_s|(H_q^{n+1} - H_p^{n+1})T_s^{n+\frac{1}{2}} \\ &+ \frac{1}{4}\Delta t\sum_{\Sigma_{sp}}s_{sp}|\Sigma_{sp}|(H_e^{n+1} - H_d^{n+1})T_s^{n+\frac{1}{2}} + \frac{1}{4}\Delta t\sum_{\Sigma_{sq}}s_{sq}|\Sigma_{sq}|(H_e^{n+1} - H_d^{n+1})T_s^{n+\frac{1}{2}}. \end{aligned}$$

Let a and b be arbitrary values such that $0 < a, b < 1$. Thanks to (1) the previous expression can be rewritten as

$$\begin{aligned} \int\int_\Omega U^{n+1} &= \frac{1}{4}\sum_{Q_{sp}}\|Q_{sp}\|\left(\mu(H_p^{n+1})^2 + 2\frac{\Delta t}{c_{sp}|\Sigma_{sp}|}H_p^{n+1}T_s^{n+\frac{1}{2}} + 2(1-a)\varepsilon(T_s^{n+\frac{1}{2}})^2\right) \\ &+ \frac{1}{4}\sum_{Q_{sq}}\|Q_{sq}\|\left(\mu(H_q^{n+1})^2 - 2\frac{\Delta t}{c_{sq}|\Sigma_{sq}|}H_q^{n+1}T_s^{n+\frac{1}{2}} + 2(1-b)\varepsilon(T_s^{n+\frac{1}{2}})^2\right) \\ &+ \frac{1}{4}\sum_{Q_{sp}}\|Q_{sp}\|\left(\frac{1}{2}\mu(1-a)(H_d^{n+1})^2 - 2\frac{\Delta t}{|S_s|}H_d^{n+1}N_s^{n+\frac{1}{2}} + \varepsilon\left(N_s^{n+\frac{1}{2}}\right)^2\right) \\ &+ \frac{1}{4}\sum_{Q_{sp}}\|Q_{sp}\|\left(\frac{1}{2}\mu(1-a)(H_e^{n+1})^2 + 2\frac{\Delta t}{|S_s|}H_e^{n+1}N_s^{n+\frac{1}{2}} + \varepsilon\left(N_s^{n+\frac{1}{2}}\right)^2\right) \\ &+ \frac{1}{4}\sum_{Q_{sq}}\|Q_{sq}\|\left(\frac{1}{2}\mu(1-b)(H_d^{n+1})^2 - 2\frac{\Delta t}{|S_s|}H_d^{n+1}N_s^{n+\frac{1}{2}} + \varepsilon\left(N_s^{n+\frac{1}{2}}\right)^2\right) \\ &+ \frac{1}{4}\sum_{Q_{sq}}\|Q_{sq}\|\left(\frac{1}{2}\mu(1-b)(H_e^{n+1})^2 + 2\frac{\Delta t}{|S_s|}H_e^{n+1}N_s^{n+\frac{1}{2}} + \varepsilon\left(N_s^{n+\frac{1}{2}}\right)^2\right) \\ &+ \frac{1}{4}\sum_{Q_{sp}}\|Q_{sp}\|\left(\frac{1}{2}\mu a(H_d^{n+1})^2 - 2\frac{s_{sp}\Delta t}{c_{sp}|S_s|}H_d^{n+1}T_s^{n+\frac{1}{2}} + \varepsilon a\left(T_s^{n+\frac{1}{2}}\right)^2\right) \\ &+ \frac{1}{4}\sum_{Q_{sp}}\|Q_{sp}\|\left(\frac{1}{2}\mu a(H_e^{n+1})^2 + 2\frac{s_{sp}\Delta t}{c_{sp}|S_s|}H_e^{n+1}T_s^{n+\frac{1}{2}} + \varepsilon a\left(T_s^{n+\frac{1}{2}}\right)^2\right) \\ &+ \frac{1}{4}\sum_{Q_{sq}}\|Q_{sq}\|\left(\frac{1}{2}\mu b(H_d^{n+1})^2 - 2\frac{s_{sq}\Delta t}{c_{sq}|S_s|}H_d^{n+1}T_s^{n+\frac{1}{2}} + \varepsilon b\left(T_s^{n+\frac{1}{2}}\right)^2\right) \\ &+ \frac{1}{4}\sum_{Q_{sq}}\|Q_{sq}\|\left(\frac{1}{2}\mu b(H_e^{n+1})^2 + 2\frac{s_{sq}\Delta t}{c_{sq}|S_s|}H_e^{n+1}T_s^{n+\frac{1}{2}} + \varepsilon b\left(T_s^{n+\frac{1}{2}}\right)^2\right). \end{aligned}$$

Therefore sufficient conditions for the total energy to be positive are, for all Q_{sp}

$$4\frac{\Delta t^2}{c_{sp}^2|\Sigma_{sp}|^2} \leqslant 8\varepsilon\mu(1-a), \quad 4\frac{\Delta t^2}{|S_s|^2} \leqslant 2\varepsilon\mu(1-a), \quad 4\frac{s_{sp}^2\Delta t^2}{c_{sp}^2|S_s|^2} \leqslant 2\varepsilon\mu a^2$$

and, for all Q_{sq}

$$4\frac{\Delta t^2}{c_{sq}^2|\Sigma_{sq}|^2} \leqslant 8\varepsilon\mu(1-b), \quad 4\frac{\Delta t^2}{|S_s|^2} \leqslant 2\varepsilon\mu(1-b), \quad 4\frac{s_{sq}^2\Delta t^2}{c_{sq}^2|S_s|^2} \leqslant 2\varepsilon\mu b^2$$

that is (c being the velocity of light such that $\varepsilon\mu c^2 = 1$)

$$c\Delta t \leqslant \frac{\sqrt{2}}{2} \times \min\left(\min_{Q_{sp}}\left[\min\left(2(1-a)^{\frac{1}{2}}c_{sp}|\Sigma_{sp}|, (1-a)^{\frac{1}{2}}|S_s|, a\frac{c_{sp}}{s_{sp}}|S_s|\right)\right], \min_{Q_{sq}}\left[\min\left(2(1-b)^{\frac{1}{2}}c_{sq}|\Sigma_{sq}|, (1-b)^{\frac{1}{2}}|S_s|, b\frac{c_{sq}}{s_{sq}}|S_s|\right)\right]\right).$$

By looking for the values a and b which maximize

$$\min\left(2(1-a)^{\frac{1}{2}}c_{sp}|\Sigma_{sp}|, (1-a)^{\frac{1}{2}}|S_s|, a\frac{c_{sp}}{s_{sp}}|S_s|\right)$$

and

$$\min\left(2(1-b)^{\frac{1}{2}}c_{sq}|\Sigma_{sq}|, (1-b)^{\frac{1}{2}}|S_s|, b\frac{c_{sq}}{s_{sq}}|S_s|\right),$$

we find the condition (15).

References

[1] K. Yee, Numerical solution of initial boundary value problems involving Maxwell's Equations in isotropic media, IEEE Trans. Antennas Propag. AP-16 (1966) 302–307.
[2] S.C. Hagness, A. Taflove, S.D. Gedney, Finite-difference time-domain methods, in: P.G. Ciarlet (Ed.), Handbook of Numerical Analysis, vol. 13, Elsevier North Holland, 2005.
[3] B.J. McCartin, J.F. Dicello, Three dimensional finite difference frequency domain scattering computation using the control region approximation, IEEE Trans. Magnetics 25 (4) (1989) 3092–3094.
[4] F. Hermeline, Deux schémas d'approximation des équations de Vlasov–Maxwell bidimensionnelles sur des maillages de Voronoi et Delaunay, Technical report: note CEA/2591 (in French), 1989.
[5] F. Hermeline, Maillage de Delaunay-Voronoi et approximation numérique de quelques équations aux dérivées partielles, Technical report: note CEA/2678 (in French), 1991.
[6] F. Hermeline, Two coupled particle finite volume methods using Delaunay–Voronoi meshes for the approximation of Vlasov–Poisson and Vlasov–Maxwell equations, J. Comput. Phys. 106 (1993) 1–18.
[7] R.A. Nicolaides, D.-Q. Wang, Convergence analysis of a covolume scheme for Maxwell's equations in three dimensions, Math. Comput. 67 (1998) 947–963.
[8] E.T. Chung, B. Engquist, Convergence analysis of fully discrete finite volume methods for Maxwell's equations in nonhomogeneous media, SIAM J. Numer. Anal. 43 (1) (1998) 303–317.
[9] J.-C. Nedelec, A new family of mixed elements in $\mathbb{R}^3$, Numer. Math. 50 (1986) 57–81.
[10] F. Assous, P. Degond, E. Heintzé, P.-A. Raviart, J. Segré, On a finite-element method for solving the three-dimensional Maxwell's equations, J. Comput. Phys. 109 (1993) 222–237.
[11] F. Assous, P. Degond, J. Segré, Numerical approximation of the Maxwell equations in inhomogeneous media by a P1 conforming finite element method, J. Comput. Phys. 128 (1996) 363–380.
[12] F. Ben Belgacem, A. Buffa, Y. Maday, The mortar finite element method for 3D Maxwell equations: first results, SIAM J. Numer. Anal. 39 (2001) 880–901.
[13] A. Buffa, Y. Maday, F. Rapetti, A sliding mesh-mortar method for a two dimensional eddy currents model of electric engines, Math. Model. Numer. Anal. 35 (2001) 191–228.
[14] F. Collino, T. Fouquet, P. Joly, A conservative space–time mesh refinement method for the 1D wave equation. Part I: construction, Numer. Math. 95 (2003) 197–221.
[15] F. Collino, T. Fouquet, P. Joly, A conservative space–time mesh refinement method for the 1D wave equation. Part II: analysis, Numer. Math. 95 (2003) 223–251.
[16] P. Joly, J. Rodriguez, An error analysis of conservative space–time mesh refinement methods for the one-dimensional wave equation, SIAM J. Numer. Anal. 43 (2005) 825–859.
[17] P. Lacoste, La condensation de la matrice masse, ou mass-lumping, pour les éléments finis mixtes de Raviart–Thomas-Nédélec d'ordre 1, C.R. Acad. Sci. Paris, Ser. I 339 (2004) 727–732.
[18] G. Mur, Compatibility relations and the finite-element formulation of electromagnetic field problems, IEEE Trans. Magnetics 30 (1994) 2972–2975.
[19] G. Mur, The fallacy of edge elements, IEEE Trans. Magnetics 34 (1998) 3244–3247.
[20] B. Jiang, J. Wu, L.A. Povinelli, The origin of spurious modes in computational electromagnetics, J. Comput. Phys. 125 (1996) 104–123.
[21] A.H. Mohammadian, V. Shankar, W. Hall, Computations of electromagnetic scattering and radiation using a time-domain finite volume discretization procedure, Comput. Phys. Commun. 68 (1991) 175–196.
[22] J.-P. Cioni, L. Fezoui, H. Steve, A parallel time-domain Maxwell solver using upwind schemes and triangular meshes, IMPACT Comput. Sci. Eng. 5 (1993) 215–247.
[23] U. Voss, C.-D. Munz, R. Schneider, A finite volume method for the instationary Maxwell equations, Z. Angew. Math. Mech. 76 (Suppl. 1) (1996) 579–580.
[24] C.-D. Munz, R. Schneider, U. Voss, A finite-volume method for the Maxwell equations in the time domain, SIAM J. Sci. Comput. 22 (2000) 449–475.

[25] Z.J. Wang, A.J. Przekwas, Yen Liu, A FV-TD electromagnetic solver using adaptive Cartesian grids, Comput. Phys. Commun. 148 (2002) 17–29.
[26] C.-D. Munz, R. Schneider, E. Sonnendrücker, U. Voss, Maxwell's equations when the charge conservation is not satisfied, C.R. Acad. Sci. Paris, Ser. I 328 (1999) 431–436.
[27] C.-D. Munz, P. Omnes, R. Schneider, E. Sonnendrücker, U. Voss, Divergence correction techniques for Maxwell solvers based on a hyperbolic model, J. Comput. Phys. 161 (2000) 484–511.
[28] C.-D. Munz, P. Omnes, R. Schneider, A three-dimensional finite-volume solver for the Maxwell equations with divergence cleaning on unstructured meshes, Comput. Phys. Commun. 130 (2000) 83–117.
[29] M. Remaki, A new finite volume scheme for solving Maxwell's system, COMPEL 19 (2000) 913–931.
[30] S. Piperno, M. Remaki, L. Fezoui, A non-diffusive finite volume scheme for the 3D Maxwell equations on unstructured meshes, SIAM J. Numer. Anal. 39 (2002) 2089–2108.
[31] L. Fezoui, S. Lanteri, S. Lohrengel, S. Piperno, Convergence and stability of a discontinuous Galerkin time-domain method for the 3D heterogeneous Maxwell equations on unstructured meshes, Math. Model. Numer. Anal. 39 (2005) 1149–1176.
[32] N. Canouet, L. Fezoui, S. Piperno, Discontinuous Galerkin time-domain solution of Maxwell's equations on locally-refined non-conforming Cartesian grids, COMPEL 24 (2005) 1381–1401.
[33] F. Assous, P. Ciarlet, P.-A. Raviart, E. Sonnendrücker, Characterization of the singular part of Maxwell's equations in a polyhedral domain, Math. Methods Appl. Sci. 22 (1999) 485–499.
[34] M. Ainsworth, J. Coyle, Hierachic *hp*-edge element families for Maxwell's equations on hybrid quadrilateral/triangular meshes, Comput. Methods Appl. Mech. Eng. 190 (2001) 6709–6733.
[35] W. Rachowicz, A. Zdunek, An *hp*-adaptive finite element method for scattering problems in computational electromagnetics, Int. J. Numer. Methods Eng. 62 (2005) 1226–1249.
[36] P. Houston, I. Perugia, D. Schötzau, Energy norm a posteriori error estimation for mixed discontinuous Galerkin approximations of the Maxwell operator, Comput. Methods Appl. Mech. Eng. 194 (2005) 499–510.
[37] L. Demkowicz, J. Kurtz, Projection-based interpolation and automatic *hp*-adaptivity for finite element discretizations of elliptic and Maxwell problems, in: ESAIM, Proceedings, electronic only, vol. 21, 2007, pp. 1–15.
[38] M. Costabel, M. Dauge, C. Schwab, Exponential convergence of *hp*-FEM for Maxwell equations with weighted regularization in polygonal domains, Math. Models Methods Appl. Sci. 15 (2005) 575–622.
[39] P. Ciarlet Jr., E. Jamelot, Continuous Galerkin methods for solving the time-dependent Maxwell equations in 3D geometries, J. Comput. Phys. 226 (2007) 1122–1135.
[40] F. Assous, P. Ciarlet jun., E. Garcia, J. Segré, Time-dependent Maxwell's equations with charges in singular geometries, Comput. Methods Appl. Mech. Eng. 196 (2006) 665–681.
[41] F. Assous, P. Ciarlet jun., J. Segré, Numerical solution to the time-dependent Maxwell equations in two-dimensional singular domains: the singular complement method, J. Comput. Phys. 161 (2000) 218–249.
[42] B. Cockburn, F. Li, C.-W. Shu, Locally divergence-free discontinuous Galerkin methods for the Maxwell equations, J. Comput. Phys. 194 (2004) 588–610.
[43] J.S. Hesthaven, T. Warburton, Nodal high-order methods on unstructured grids. I. Time-domain solution of Maxwell's equations, J. Comput. Phys. 181 (2002) 186–221.
[44] G.B. Jacobs, J.S. Hesthaven, High-order nodal discontinuous Galerkin particle-in-cell method on unstructured grids, J. Comput. Phys. 214 (2006) 96–121.
[45] R.S. Falk, G.R. Richter, Explicit finite element methods for symmetric hyperbolic equations, SIAM J. Numer. Anal. 36 (1999) 935–952.
[46] P. Monk, G.R. Richter, A discontinuous Galerkin method for linear symmetric hyperbolic systems in inhomogeneous media, J. Sci. Comput. 22–23 (2005) 443–477.
[47] F. Hermeline, Une méthode de volumes finis pour les équations elliptiques du second ordre, C.R. Acad. Sci. Paris, Ser. 1 326 (1998) 1433–1436.
[48] F. Hermeline, A finite volume method for the approximation of diffusion operators on distorted meshes, J. Comput. Phys. 160 (2000) 481–499.
[49] F. Hermeline, Approximation of diffusion operators with discontinuous tensor coefficients on distorted meshes, Comput. Methods Appl. Mech. Eng. 192 (2003) 1939–1959.
[50] F. Hermeline, Approximation of 2-D and 3-D diffusion operators with variable full tensor coefficients on arbitrary meshes, Comput. Methods Appl. Mech. Eng. 192 (2007) 2497–5326.
[51] K. Domelevo, P. Omnes, A finite volume method for the Laplace equation on almost arbitrary two-dimensional grids, ESAIM: Math. Model. Numer. Anal. 39 (2005) 1203–1249.
[52] S. Delcourte, K. Domelevo, P. Omnes, Discrete duality finite volume method for second order elliptic problems, in: F. Benkhaldoun, D. Ouazar, S. Raghay (Eds.), Finite Volumes for Complex Applications IV, Hermes Science publishing, 2005, pp. 447–458.
[53] S. Delcourte, K. Domelevo, P. Omnes, A discrete duality finite volume approach to Hodge decomposition and div–curl problems on almost arbitrary two-dimensional meshes, SIAM J. Numer. Anal. 45 (3) (2007) 1142–1174.
[54] A. Bossavit, Discretization of electromagnetic problems: the "generalized finite differences" approach, in: P.G. Ciarlet (Ed.), Handbook of Numerical Analysis, Vol. 13, Elsevier North Holland, 2005.
[55] B. Andreianov, F. Boyer, F. Hubert, Discrete duality finite volume schemes for Leray–Lions-type elliptic problems on general 2D meshes, Numer. Methods Partial Differ. Equations 23 (1) (2007) 145–195.
[56] C. Chainais-Hillairet, Finite volume schemes for two dimensional drift-diffusion and energy-transport models, in: F. Benkhaldoun, D. Ouazar, S. Raghay (Eds.), Finite Volumes for Complex Applications IV, Hermes Science Publishing, 2005, pp. 13–22.
[57] C. Chainais-Hillairet, Discrete duality finite volume schemes for two-dimensional drift-diffusion and energy-transport models, Int. J. Numer. Meth. Fluids, in press, doi:10.1002/fld.1393.
[58] C. Pierre, Modélisation et simulation de l'activité électrique du cœur dans le thorax, analyse numérique et méthodes de volumes finis, Ph.D. Thesis (in French), University of Nantes, France, 2005.
[59] F. Hermeline, A finite volume method for solving Maxwell's equations in inhomogeneous media on arbitrary meshes, C.R. Acad. Sci. Paris, Ser. 1 339 (2004) 893–898.
[60] F. Hermeline, Une méthode automatique de maillage en dimension *N*, Ph.D. Thesis (in French), Université P. et M. Curie Paris 6, Paris, 1980.
[61] F. Hermeline, Triangulation automatique d'un polyèdre en dimension *N*, Revue Automatique Informatique Recherche Opérationnelle, Analyse Numérique/Numer. Anal. 16 (1982) 211–242 (in French).
[62] P.L. George, F. Hermeline, Delaunay's mesh of a convex polyhedron in dimension *d*. Application to arbitrary polyhedra, Int. J. Numer. Methods Eng. 33 (1992) 975–995.
[63] P.L. George, H. Borouchaki, Delaunay Triangulation and Meshing. Applications to Finite Elements, Hermes Science Publishing, Paris, 1998.
[64] S. Piperno, L^2-stability of the upwind first order finite volume scheme for the Maxwell equations in two and three dimensions on arbitrary unstructured meshes, M2AN, Math. Model. Numer. Anal. 34 (2000) 139–158.
[65] N.K. Madsen, R.W. Ziolkowski, Numerical solution of Maxwell's equations in the time domain using irregular nonorthogonal grids, Wave Motion 10 (1995) 583–596.
[66] R. Le Martret, C. Le Potier, Finite volume solution of Maxwell's equations in nonsteady mode, La Recherche Aérospatiale 5 (1994) 329–342.
[67] N.K. Madsen, Divergence preserving discrete surface integral methods for Maxwell's curl equations using non-orthogonal unstructured grids, J. Comput. Phys. 119 (1995) 34–45.